

Time-series Analysis of GNSS Processing Strategies

*Estimating Tidally Modulated Ice-flow motion of
Priestley Glacier, East Antarctica*

Bachelor thesis
submitted in partial fulfilment of the requirements
to obtain the academic degree of
“Bachelor of Arts” **OR** “Bachelor of Science”
In Liberal Arts and Sciences
at the University College Freiburg
of the Albert-Ludwigs-University Freiburg

submitted by

First and Last Name: Ka Hei Pinky, Chow

Matriculation Number: 4355255

Majoring in: Earth and Environmental Science

First examiner (supervisor): Juniorprof. Dr. Reinhard Drews

Second examiner: Prof. Dr. Stefan Hergarten

Word count: 11184

Date of submission: 20/10/2020

Abstract

Previous research has revealed that ocean tides are imprinted on the ice motion of grounded glaciers, yet the detailed ice-stream mechanics are uncertain. Further studies rely on accurate measurement of glacial dynamics on sub-daily timescales, often via a Global Navigation Satellite System (GNSS). As the implementation of GNSS processing strategies imposes variations in results, the present study aims to evaluate the performance of multiple GNSS processing schemes and platforms, investigating their strengths and limitations. It aims to optimize the sub-daily positioning solution to analyze 10-day GNSS data at the grounding zone of Priestley Glacier, Antarctica. The accuracy and precision from different strategies are calculated and the tidal signals are reconstructed using Singular Spectrum Analysis (SSA). Comparative analysis reveals that precise point positioning (PPP) mode and CSRS-PPP processing application demonstrate the highest performance. At the control station, CSRS-PPP shows a variance below 0.5 millimetres for all dimension. Both diurnal and semi-diurnal tidal signals are best preserved with this optimal processing strategy.

Keywords: global navigation satellite systems; precise point positioning; grounding zone dynamics; tidal modulation

TABLE OF CONTENTS

LIST OF TABLES	4
LIST OF FIGURES.....	5
LIST OF ABBREVIATIONS	6
1. INTRODUCTION.....	7
a. Antarctic Ice-Sheet Dynamics and Sea-level Rise.....	7
b. GNSS Application	9
c. Research Aims and Objectives.....	10
d. Field Location and Data Source	11
2. THEORETICAL BACKGROUND AND LITERATURE REVIEW	11
a. Glacier Hydrological System	11
b. Basal Motion	12
c. Mass Balance	13
d. Grounding zone dynamics.....	14
e. Grounding zone mapping	16
f. Tidally-induced ice motion	17
g. Modelling effort	18
h. Remote Sensing techniques: Principles of Interferometry and GNSS	20
i. Remote Sensing Application on ice-flow measurement	23
j. Performance deviation among GNSS strategies	25
3. METHODOLOGY	26
a. Fieldwork	26
b. Data Processing	27
c. Dynamic Time Warping (DTW)	29
d. Singular Spectrum Analysis (SSA)	29
4. RESULTS AND DISCUSSION	32
a. Accuracy	32
b. Precision	33
c. PPP versus DGNSS	37
d. Vertical Displacement	38
e. Spatial structure of the ice motion.....	39
f. Observations of Tidal Modulation	41
5. CONCLUSION	46
REFERENCES.....	49
APPENDICES.....	58
a. Appendix A: RTKLIB/PPP configuration	58
b. Appendix B: Overview of GNSS processing results.....	59
c. Appendix C: Statistical information of GNSS solutions	62
d. Appendix D: Results of SSA analysis	63

LIST OF TABLES

Table 1 – Major sources of GNSS range error	22
Table 2 – The applied GNSS strategies	31
Table 3 – Positioning accuracy	33
Table 4 – Applied options for testing configuration in RTKLIB/PPP	58
Table 5 – Positioning statistics.....	62

LIST OF FIGURES

Figure 1 – Map of the velocity field in Antarctica	8
Figure 2 – Visualization of features and concepts in glacial dynamics	16
Figure 3 – Working principle of ground-based/ terrestrial radar interferometry	21
Figure 4 – Trilateration of GNSS positioning	22
Figure 5a – Working principle of local DGNSS	23
Figure 5b – Working principle of WADGNSS	23
Figure 6 – Map of the GNSS field stations	26
Figure 7 – Positioning results.....	33
Figure 8 – FFT periodogram of the frequency distribution	35
Figure 9 – Bootstrapping convergence.....	37
Figure 10 – The similarity of the time series	40
Figure 11 – Vertical variations.....	44
Figure 12 – Horizontal velocities	44
Figure 13 – Positioning solutions at Blake.....	59
Figure 14 – Positioning solutions at Hillary.....	59
Figure 15 – Positioning solutions at Shirase	60
Figure 16 – Positioning solutions at Tuati	60
Figure 17 – Positioning solutions at Base	61
Figure 18 – GNSS solutions of all stations	61
Figure 19 – SSA reconstruction at Shirase.....	63
Figure 20 – SSA reconstruction at Tuati.....	63
Figure 21 – SSA reconstruction at Hillary	64
Figure 22 – SSA reconstruction at Blake	64

LIST OF ABBREVIATIONS

APPS	the Automatic Precise Positioning Service
C/A code	Coarse Acquisition code
CoM	Centre of Mass
CSRS	the Canadian Spatial Reference System
DD	Double Difference
DEM	Digital Elevation Model
DOP	Dilution Of Precision
DOY	Day Of Year
ERS	the European Remote Sensing satellite
FFT	Fast Fourier Transform
GAPS	the GPS Analysis and Position Software
GBRI	Ground-Based Radar Interferometry
GLONASS	Global Navigation Satellite System
GMSL	Global Mean Sea Level
GNSS	Global Navigation Satellite System
GPS	Global Positioning System
GRACE	the Gravity Recovery And Climate Experiment
Grad	Horizontal Gradient
GUI	Graphical User Interface
ICESat	Ice Cloud and land Elevation Satellite
IF	Ionospheric-Free
IGS	the International GNSS Service
InSAR	Interferometric Synthetic Aperture Radar
LS	Least Square
MOA	Mosaic Of Antarctica
MODIS	the Moderate Resolution Imaging Spectroradiometer
MSf	lunisolar Synodic Fortnightly
P code	Precise code
PPP	Precise Point Positioning
RMS	Root-Mean-Square
RMSE	Root-Mean-Square Error
SAR	Synthetic Aperture Radar
SSA	Singular Spectrum Analysis
Utide	Unified Tidal analysis and prediction
WADGNSS	Wide Area Differential Global Navigation Satellite System
ZTD	Zenith Tropospheric Delay

I. Introduction

a. Antarctic Ice-Sheet Dynamics and Sea-level Rise

To correctly measure Antarctic ice-sheet flow is a key concern for current research as the ice motion underpins complex dynamics which help to project future sea-level rise. *Global mean sea level (GMSL)* changes depending on the volume of the ocean which is determined by both its density and mass: Between 1993 and 2010, $1.1 \pm 0.3 \text{ mm yr}^{-1}$ of the sea-level change are the consequence of thermal expansion and $1.84 \pm 0.41 \text{ mm yr}^{-1}$ caused by increasing water mass (Church et al., 2013). Among those, 0.27 mm yr^{-1} are contributed by the Antarctic ice sheet. Apart from the mass exchange between the continent and ocean, the sea level will also be altered by the glacial isostatic adjustment and other anthropogenic processes. In Antarctica, accumulation, calving and ice flow into floating ice shelves, i.e. discharging solid ice into the ocean, are predominant for its mass budget, while surface melting and runoff are negligible (about 1% of the total mass gain from snowfall).

The Antarctic ice sheet has an average ice thickness of 2200 m and a surface area of 14 million km^2 , which amounts to ~90% of the glacier ice and can potentially raise the GMSL by 70 m if it melts (Baumhoer et al., 2018; Rémy & Frezzotti, 2006). It is, nevertheless, challenging to calculate its mass balance due to its hostile environment, extreme climate, complex rheology, poorly known boundary conditions and past climate forcing. Antarctic ice-sheet dynamics are influenced by oceanic and atmospheric forcing, of which understandings are required to accurately project the future global sea level (Pritchard et al., 2012). Ice sheets, on another hand, also perturb the atmospheric circulation as well as the marine hydrological cycle, leading to influences on the global climate (Cuffey & Paterson, 2010). Ice sheet changes are driven by numerous factors such as snowfall, air temperature, the marine termini of ice streams, surface melt as well as the condition of ocean water. The ice-flow velocity in

Antarctica from different satellite measurements has been derived and mapped by E. Rignot et al. (2011), shown in Figure 1. The ice-flow velocity gradually speeds up towards the periphery, particularly on the ice streams, and peaks on ice shelves. In Antarctica, the ice sheet can be divided into Antarctic Peninsula, West Antarctica, and East Antarctica. While the Antarctic Peninsula is heavily influenced by the ocean and dominated by surface melting, East Antarctica has a higher elevation with an exceptionally cold and dry climate. The West is warmer and receives more snowfall. For both East and West Antarctica, most of the *ablation*, i.e. loss of ice and snow mass, is caused by calving and basal melting. The annual surface mass budget of ice shelves accounts for 21% of the whole ice sheet although ice shelves only amount to 12.5% of the Antarctic Ice Sheet.

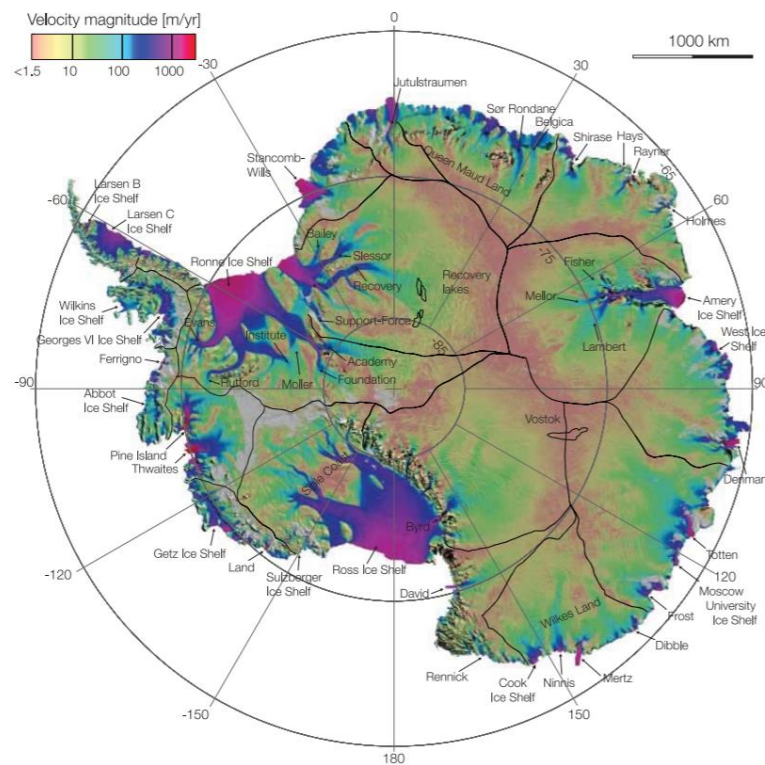


Figure 1. Map of the velocity field in Antarctica (E. Rignot et al., 2011).

Under climate change, oceanic and atmospheric warming threatens the stability of the Antarctic floating ice shelves which reduces the buttressing force on the ice sheet, accelerating the ice flow (Joughin & Alley, 2011). The interactions between ocean tides and

ice sheets are of particular concern with respect to its important role in the oceanic processes. At the marine margin, rising and falling ocean tides modulate the lateral motion of grounded ice sheets and floating ice shelves, which is revealed by multiple geodetic and geophysical methods such as Global Navigation Satellite System (GNSS) and glacier seismology (Langley et al., 2017). The resultant ice flow variations are reported to be either sinusoidal or stick-slip (Bindschadler et al., 2003; Rosier et al., 2017). Tidal signals on ice sheets are reported on annual, semi-annual, fortnightly, diurnal and semi-diurnal periods and the patterns depend on specific locations (Murray et al., 2007; Padman et al., 2018). It is suggested that such tidal modulations influence ice shelf basal melting, the production and export of meltwater and cause non-linear effects of grounding line migration (Begeman et al., 2020; Rosier et al., 2014). Since the ice sheet responses to ocean tides are complex, extracting tidal signals from ice-shelf flows can unfold the hidden influences of the pinning points on ice-stream flow, which are difficult to observe at the surface (Robel et al., 2017). The ice-flow measurement has most commonly resorted to different processing strategies of GNSS, of which the suitability will be examined in this study.

b. GNSS Application

Global Navigation Satellite System (GNSS) refers to the satellite constellation in space which transmits positioning and timing data to the receivers on the ground for determining location (P. Teunissen & Montenbruck, 2017). This space-based geodetic instrument has been extensively applied in many areas, including air positioning, static and kinematic positioning, and sea surface monitoring (He, 2015). Apart from the Global Positioning System (GPS) developed by the United States, there are also other satellite navigation systems such as the Global Navigation Satellite System (GLONASS) and Galileo. GNSS positioning modes vary from pseudorange-based/ code-based to carrier-phase-based approaches and their accuracy ranges from meters to subcentimeter, limited by the uncertainties of satellite orbits, clock

information and atmospheric propagation delay (Langley et al., 2017). Code Differential Positioning (DGNSS) and Precise Point Positioning (PPP) are the most commonly used data processing strategies in the field (eg. Brunt & MacAyeal, 2014; Horgan et al., 2013; Murray et al., 2007; Rosier et al., 2017). Whilst DGNSS obtains corrections from the reference station, PPP requires no base station, uses carrier-phase measurements and corrects the errors with additional GNSS data products (Langley et al., 2017). GNSS data can be handled with various academic software, commercial software and web-based online processing services, providing solutions of different accuracies depending on the implemented algorithms (Martín et al., 2012).

c. Research Aims and Objectives

Concerning extensive use of GNSS in studying tidally modulated ice flow, key questions that have been motivated by prior research are: How important is the role of GNSS processing strategies in the observed ice-flow variations? Are the documented comparison in the previous literature representative for the Antarctic context? What are the critical factors in GNSS processing phase to perform successful tidal analyses? As detailed observations of tidal modulation allow for valuable insights into the involved ice dynamics, it is favourable to obtain positioning results in a high temporal resolution. An examination of GNSS strategies concerning their accuracy and precision is thus called-for. Moreover, as the uses of different GNSS options produce varying results, investigating their strengths and limitations can facilitate informed decision making, as well as comprehension of the potential uncertainties in the analyses.

In addition, previous studies rely on existing toolboxes and conventional approaches such as the least square method to identify cyclical and seasonal variations. As research suggested Singular Spectrum Analysis (SSA) as a preferable option to extract modulated oscillations in time series (Q. Chen et al., 2015), the present study also explores its potential in the tidal

analyses. To address the aforementioned questions, field data of five stations at Priestley Glacier of 10 days is applied to The Canadian Spatial Reference System (CSRS) PPP, magicGNSS, RTKLIB for PPP processing, and RTKLIB for differential GNSS processing to assess their performance. The main emphasis is to inspect their fitness to measure vertical ice displacement and lateral velocity across the grounding line in diurnal and semidiurnal tidal frequencies. The data is analyzed for the important information about ice-flow variations, which will be described in this paper.

d. Field Location and Data Source

The GNSS data are collected at Tuati, Shirase, Blake, and Hillary stations which are located at Priestley Glacier along the flowline, across the grounding line where ice transits from the grounded ice sheet to the floating ice shelf. Priestley Glacier originates at the margin of Victoria Land in East Antarctica, which fronts the western side of the Ross Sea as well as the Ross Ice Shelf (*Priestley Glacier*, 2012). The glacier flows across the Transantarctic Mountains which divides East and West Antarctica and ends up at Nansen Ice Sheet. This paper presents a compilation of GNSS observations which were made from 5th to 15th November in the early summer in 2018. It is to measure the response of the outlet glacier to ocean tides with both high spatial and temporal resolutions.

II. Theoretical Background and Literature Review

a. Glacier Hydrological System

The flow of water through glaciers creates a complex hydrological system with multiple features that is relevant to the glacier hydrology (Cuffey & Paterson, 2010). Meltwater forms channels on the glacier surface and flows into the subsurface through cracks and moulins. In summer, the meltwater channels at the ablation zone resemble a river system and can form

meltwater lakes if the slope is gentle. The water flow at the glacier bed depends on parameters such as pressure, conductivity and turbidity: it is distributed extensively in thin films, small cavities and small channels. The basal water system can influence basal slip motion through high water pressure which causes deformation of the basal sediments and lubrication at the interface, which can speed up the ice flow and open up cavities. In Antarctica, thick ice and low accumulation rates warm up the base of ice sheets which allow the formation of its 150 subglacial lakes, including Lake Vostok, with a remarkable area of 15,690 km².

b. Basal Motion

Basal Motion refers to the combined motion of sliding and bed deformation, both occurring in a thin layer beneath the glacier (Cuffey & Paterson, 2010). It is important to predict the responses of glaciers to mass balance changes and comprises the relationship between basal velocity, shear stress, bedrock topography and other bed properties. The movements of glaciers can be explained by three different mechanisms, namely *basal sliding*, *plastic deformation* and *bed deformation*, with the latter two often occurring in parallel. Sliding behaviour differs on deformable and rigid beds. It produces shear stress to oppose the motion of the glacier and depends on the lubrication represented by drag factor ψ in the equation:

$$\tau_b = \psi u_b$$

with basal shear stress τ_b and rate of slip u_b . On a rigid bed, sliding is governed by mechanisms such as *regelation* which describes the meltwater flow around the bump and refreezes at the interface, and *enhanced creep* which refers to the viscous ice deformation. In contrast, deformable beds allow the sliding of ice along the top of the substrate and deformation within it. On another hand, plastic deformation entails both *intracrystalline gliding*, the dislocation of layers within ice crystals, and *recrystallization*, in which crystal boundaries resize and reshape.

c. Mass Balance

The mass of ice in the glacier changes by mass transfer between the glacier, the atmosphere, the land and groundwater, in the form of both ice and liquid water (Cuffey & Paterson, 2010). It can operate at the surface, within the ice and at the base. Snowfall, avalanching, melt, sublimation, as well as calving, are the most common mass exchange processes. Many glaciers have a mass surplus in winter and a mass deficit in summer. The specific balance also varies from region to region: the *accumulation zone* comprises the mass surplus and the *ablation zone* comprises the mass deficit. In most drainage basins in Antarctica, the accumulation zone extends to the ice margin where *calving*, the breaking of ice mass from the margins of glaciers or ice shelves, contributes to the mass loss. The mass of the glacier can also be redistributed by ice flow, which controls the rate of mass loss by calving and can be influenced by the topography, basal conditions as well as the thickness of the glacier (Cuffey & Paterson, 2010; Siegfried et al., 2016). Consequently, the glacier expands or contracts, and thus advances or retreats. Basal mass balance is of particular importance as the interactions between the basal hydrological processes and the ocean tides may play a critical role on water pressure and sliding near the grounding zone which further influences the GMSL (Cuffey & Paterson, 2010). The heat source of the basal ice comes from geo-thermal and ice-friction sources. *Basal melting* occurs with a rate defined by

$$\dot{b}_b = -\frac{E_b}{\rho_i L_f} \quad (\text{m yr}^{-1} \text{ of ice}).$$

where \dot{b}_b , ρ_i , L_f and E_b denote the mass balance at the glacier base, density of ice, latent heat of fusion and net supply rate of energy (i.e. < 0) respectively. The normal base melting rate is around several millimetres although it can be much higher where geothermal energy concentrates or beneath floating ice shelves since ocean circulation acts as a heat pump.

Particularly high basal melt rates have also been found near the grounding line of Pine Island Glacier.

Calving is another important process of mass loss in Antarctica, which accounts for over 90% of the ablation. It is caused by the initiation of fractures and their propagation, and is heavily affected by the fracturing and thinning of ice. An empirical relationship between the calving rate and its factors is defined as

$$\dot{c} = k_c H_w,$$

where k_c is a coefficient and H_w denotes water depth at the terminus divided by the width of the ice front. It is also influenced by ocean conditions. Both ice flow and calving accelerate when the ice front goes beyond a specific critical thickness. Meanwhile, calving of an ice shelf is governed by the stretching flow along the shelf and the shear on the shelf sides.

d. Grounding zone dynamics

Glaciers can be broadly defined as all ice-bodies which originate from snowfall accumulation, whereas an *ice sheet* is ice masses of continental-scale which are mostly grounded on bedrock (Cuffey & Paterson, 2010; Padman et al., 2018). Ice sheets flow towards the ocean via *ice streams* and outlet glaciers, eventually advancing into water by forming a floating *ice tongue* or *ice shelf*, which directly contributes to the rise of GMSL (Goldberg, 2016). The transport of ice mass heavily concentrates in ice streams and goes across the *grounding line*, a point at which glaciers begin to float and where the weight of the water column it occupies equals the weight of ice, i.e.

$$\rho g H = \rho_w g D$$

where ρ , ρ_w , H , and D denote average ice density, the density of the seawater, ice thickness, and bedrock depth respectively. The position and migration of the grounding line are critical

to the ice-sheet dynamics (Walker et al., 2013). For example, the retreat of the grounding line in the West Antarctica Ice Sheet would exacerbate the imbalance owing to its reduced surface area and higher depth (Goldberg, 2016). However, ice shelves could impose resistive force to slow down the outlet streams, which is known as *buttressing*. Buttressing becomes more effective with narrow, thick and long ice shelves, and can either originate from the rigid sidewalls, ice rise or ice rumples. The melting of ice shelves will speed up the ice stream flows, lead to the loss of buttressing and damages its structural stability (Dupont & Alley, 2005; Goldberg, 2016). With buttressing, boundary conditions at the ice-shelf front become an important factor for the stability of the grounding line (Haseloff & Sergienko, 2018).

Ocean tides are the result of gravitational dynamics of the Earth-Moon-Sun system, as well as the rotation of the earth, which lead to the oscillations of the ocean's surface around mean sea level at certain frequencies, particularly the diurnal and semidiurnal ones, depending on the specific location (Padman et al., 2018). At the grounding zone where the grounding line lies, ocean tides induce periodical responses on the ice shelves and grounded ice, which alters the ice-sheet dynamics through ocean mixing, sedimentation, and ecosystem behaviour. Tidal mixing enhances basal melting by changing the hydrographic characteristics of the water mass. It modifies the production, concentration, and melting of sea ice, as well as causing the formation of crevasse by weakening the mechanical structure of the ice shelves.

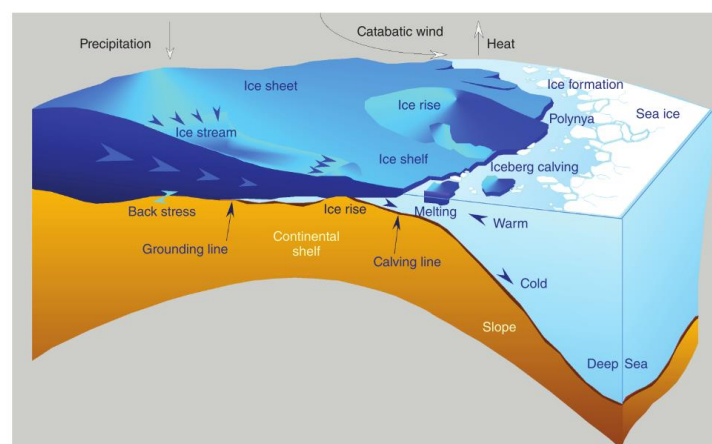


Figure 2. Visualization of features and concepts in glacial dynamics (Goldberg, 2016)

e. Grounding Zone Mapping

The major scientific questions concerning the Antarctic ice sheet are its mass balance, stability, dynamics, and past climate reconstruction, which require mapping, as well as measurements of the surface conditions, ice motions and internal properties (Thomas, 1985). Precisely mapping the ice sheet and grounding zone is critical for further understanding of the rheology and morphology of the glaciers. Eric Rignot (1998) employed satellite synthetic aperture radar interferometry using the data from the European Remote Sensing satellite (ERS) to identify the limit of tidal flexing of Rutford Ice Stream and Carlson Inlet. After the Ice Cloud and Land Elevation Satellite (ICESat) was launched in 2003 for more precise measurement (Brenner et al., 2007), Fricker et al., (2009) had developed a benchmark map for the Amery Ice Shelf Grounding Zone, the largest ice shelf in East Antarctica, using a repeat-track analysis of the ICESat data. They located several new features of the ice shelf, including the landward limit of flexure. The results are then compared to the data from the visible-band imagery and interferometric synthetic aperture radar (InSAR). Brunt et al. (2010) mapped the grounding zone of the Ross Ice Shelf in Antarctica with the same method and found out deviations in the scale of kilometres compared to MODIS MOA imagery and DEM. They concluded that the success of ICESat analysis is limited by the spacing of ground tracks, surface roughness, tidal range, and cloud cover. A similar methodology was applied to the grounding zone of the Filchner-Ronne Ice Shelf for identifying ice plains and the migration of the grounding line during the tidal cycle (Brunt et al., 2011).

f. Tidally-induced ice motion

Apart from mapping glacial features, tidal modulations have been extensively observed in the lateral motion of the ice in Antarctica, from ice front to far inland of the grounding line (Padman et al., 2018; Rosier & Gudmundsson, 2016). Ocean tides account for major

variabilities of ice-sheet motion: It is suggested that tides accelerate the ice flow via nonlinear effects of grounding line migration, as well as altering subglacial hydrology (Begeman et al., 2020). Hypotheses for the explanation includes changes in driving stress, in force balance, in frictional drag, and variations in buttressing (Padman et al., 2018). Brunt et al. (2010) associated the diurnal variations in ice displacements at the front of the Ross Ice Shelf with tidal forcing on ice shelf as a whole: The horizontal ice flows are found to be heavily modulated by the spring-to-neap cycle, diurnal and semi-diurnal tides, as well as possibly other long-period tides. Fortnightly, diurnal and semi-diurnal modulations in horizontal ice-flow velocity are also observed on the Larsen C ice shelf (King et al., 2011). Makinson et al. (2012) suggested the response of ice shelves to tidal forcing might be elastic: they recorded movement of the Ronne Ice Shelf to detect diurnal and semi-diurnal tidal signals. Results indicate that when tilted by tidal slopes, ice shelves mainly show elastic response to tidal forcing, and transmit stress further upstreams to the grounding lines. Similarly, Cooley et al. (2019) revealed tidally modulated ice flows near the grounding zone of Beardmore Glacier from InSAR data, seismic data and GPS measurements, revealing that the variations of horizontal flow are the most significant near the grounding line and decrease downstream. The effects of tidal modulations widely extend on the ice sheet: they are reported not only on the Antarctic free-floating ice shelves, but also at the ice streams. Anandakrishnan et al. (2003) provided an insight into the basal mechanics of tidal modulation: They investigated the tidal influences on the flow of the Bindschadler Ice Stream (formerly ice stream D) by analysing GPS data over 24 days using PPP algorithms implemented in GIPSY. The results demonstrated dramatic tidal-induced variations in ice flow at all stations, in which the strongest response occurs at the grounding line. The responses to tidal forcing are also subjected to delays of hours, depending on the relative position to the grounding line. The response is found to be non-linear and is explained by the viscous behaviour of the ice-stream

bed associated with varied basal shear stress. Gudmundsson (2006) demonstrated tide-induced fortnightly variations with changing amplitudes depend on the distance from the grounding line, by calculating kinematic GPS positions over seven weeks on Rutford Ice Stream, West Antarctica. Murray et al. (2007) further revealed tidal modulations at semi-diurnal, diurnal, two-weekly, semi-annual, and annual frequencies by collecting over 2-year GPS data upstream of the same grounding line using PPP. It is confirmed by Rosier et al. (2017), who collected a new GPS dataset and demonstrated flow modulations also found on Evans, Talutis, Institute, and Foundation ice streams. It was found that the fortnightly modulated ice flow is not present in the tidal forcing, but acts as a non-linear response to the ocean tides.

g. Modelling effort

In order to understand the fundamental mechanism of the tidal-modulated ice flows, extensive effort has been put into developing a representative model to reproduce the observed signals over tidal timescales. Reeh et al. (2003) suggested that instead of the previously applied elastic-beam theory, the tidal flexure zone of Nioghalvfjærdsfjorden glacier can be better explained by the Burgers rheological model. King et al. (2011) fitted an ice stream model to various tidal frequencies for Rutford Ice Stream to investigate multiple model parameters: Both semi-annual and fortnightly signals were accurately reproduced and approximately 5% of the mean flow originates from the non-linear response to tide-induced basal shear stress. On another hand, Gudmundsson (2011) conducted a numerical modelling experiment by applying the Weerman type basal sliding law to investigate basal control on the response of ice-streams to ocean tides. Tidal analysis reveals lunisolar synodic fortnightly (MSf) tidal signals reduce upstream from the grounding line which can be potentially explained with a non-linear viscous sliding law. However, models might differ regarding the characters of the ice stream: Walker et al. (2012) developed a model to explain the tidal modulated ice flow of

Bindschadler Ice Stream and demonstrated its different behaviours of the basal flow law compared to Rutford Ice Stream. The same conclusion was made by Walker et al. (2014) who applied combined models of ice-shelf flexure and ice-stream response to perturbations on Bindschadler Ice Stream. Brunt & MacAyeal (2014) offers a view of a viscoelastic model for explanation: they scrutinize the basal friction and the mechanism of tidal influence on ice-shelf motion by fitting the GPS data into two hypotheses of direct and indirect responses of ice shelves to tidal forcing: the temporal variations of the response suggests a combination of both viscous and elastic deformation. It is supported by Wild et al. (2017), who examined the validity of both elastic and viscoelastic models for the grounding zone flexure over tidal timescales by studying the effects of ice rheology on the models at the Southern McMurdo Ice Shelf. To explain the fortnightly variations of ice flow at Rutford Ice Stream, Robel et al. (2017) also used a viscoelastic model to reproduce the signals, demonstrating the potential mechanism of asymmetric buttressing stress and hydrostatic stress variations. It is important to understand how tidal forcing implemented in the models also influences the outcome: Rosier & Gudmundsson (2016) distinguished between damming, flexural, and hydrological tidal forcing in models and conclude that they offer different representations and relevance to the observations.

Furthermore, previous studies hypothesized tidal basal shear variations to explain the tidal modulation of the ice flow: For example, by applying a 3-D viscoelastic full-Stokes model to ice-stream flow, Rosier et al. (2015) demonstrated the non-linearity of the ice-stream response and revealed the coupling between subglacial water pressure variations induced by tides and basal sliding for representing the modulated ice-flow velocity. Tsai & Gudmundsson (2015) confirmed the asymmetric and nonlinear nature of the grounding line migration by assuming migration as an elastic fracture problem forced by tidally varying water pressure at the interface. It is shown that pressure perturbations in a subglacial drainage system can transmit

tens of kilometres if the system is very hydraulically conductive (Rosier & Gudmundsson, 2016). Measuring how tidal ocean pressure varies at the grounding zone of Ross Ice Shelf, Begeman et al. (2020) further hypothesized seawater being pumped into the subglacial environment by high ocean pressure which affects basal crevassing and the production of meltwater.

h. Remote Sensing Techniques: Principles of Interferometry and GNSS

In those aforementioned research studies concerning Antarctic ice dynamics, interferometry and GNSS are typically applied. In *interferometry*, phase preservation of SAR is used to extract surface velocity from an interferogram which can be acquired along-track. *Ground-based radar interferometry (GBRI)* is commonly used for monitoring small areas in short term: it utilizes a microwave beam to detect displacement between transmitted and received waves in terms of phase difference, which is defined as

$$\Delta\phi = \Delta\phi_{\text{disp}} + \Delta\phi_{\text{atm}} + \Delta\phi_{\text{noise}}$$

where $\Delta\phi_{\text{disp}}$, $\Delta\phi_{\text{atm}}$, and $\Delta\phi_{\text{noise}}$ denote possible displacement, changes in atmospheric conditions, and phase noise contribution (Pieraccini & Miccinesi, 2019).

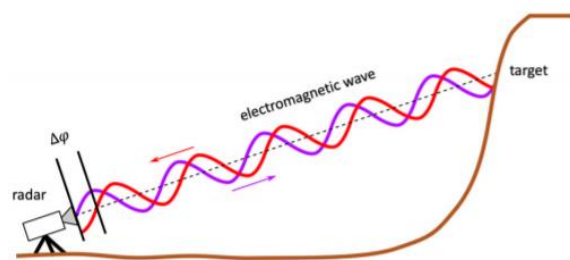


Figure 3. Working principle of ground-based/ terrestrial radar interferometry (Pieraccini & Miccinesi, 2019).

GNSS is a space-borne measurement relying on calculated distances to satellites via navigation messages (Dawoud, S., 2012). The system can be divided into space, control, and user segment. The receiver obtains navigation messages at certain frequencies (L1 and L2 in

GPS) broadcasted by the satellites and calculates the transit time. With at least four satellites, four unknowns, namely latitude, longitude, height and time synchronization (Δt), can be solved for positioning. For GPS, there is coarse acquisition (C/A) code and precise (P) code: the former is modulated on L1, whereas the later is modulated on both frequencies. The navigation is encoded with subframes containing the satellite state, satellite ephemeris, almanac data and health data. The position is then determined based on 3D trilateration by calculating the unknown receiver position vector and pseudorange p_i which is defined by

$$p_i = \sqrt{((X_i - x)^2 + (Y_i - y)^2 + (Z_i - z)^2)} + c \cdot \Delta t$$

The receiver position given in Cartesian coordinates is then transformed into the geodetic system WGS-84. The main sources of positioning errors are shown in Table 1. GNSS can be based on either code or carrier phase: while code-based GNSS determines the travel time of a signal by comparing the pseudo-random codes which allow out-of-phase matching, carrier-phase-based GNSS moves on to match the measurements based on the more precise carrier frequency.

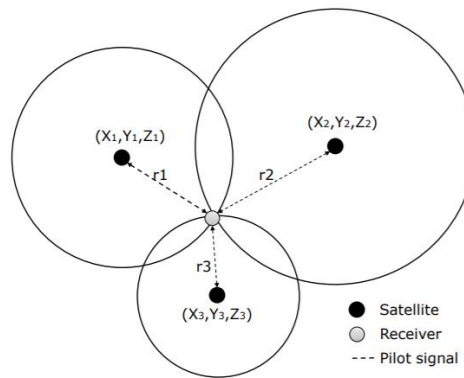


Figure 4. Trilateration of GNSS positioning, (X, Y, Z) denotes the position of the satellites (Dawoud, S., 2012).

Error Source	Error Magnitude
Ionosphere	7 meters
Troposphere	0.6 meters
Ephemeris error	2-3 meters
Satellite clock error	1-2 meters
Multipath	1-2 meters (highly dependent on environment)
Receiver noise	1-2 meter

Table 1. Major sources of GNSS range error (Dawoud, S., 2012).

One possibility for GNSS positioning is code-based DGNSS which largely reduces orbit errors and atmospheric delays based on spatial correlation (P. Teunissen & Montenbruck, 2017). Its error is approximately 1 to 3 m, depending on multipath errors and Dilution of Precision (DOP), which refers to the interference between two radio waves and the geometry of the satellite constellation, respectively. In code-based local DGNSS, a reference station with the known position is used to transmit corrections to the rover receivers. The reference station should be relatively close to the rover for both stations to share the same set of visible satellites. The accuracy can be further improved if more reference stations are provided (i.e. WADGNSS) or if an ionosphere model is available. For example, the Klobucher model is suggested to reduce ionospheric bias by 50% to 80%.

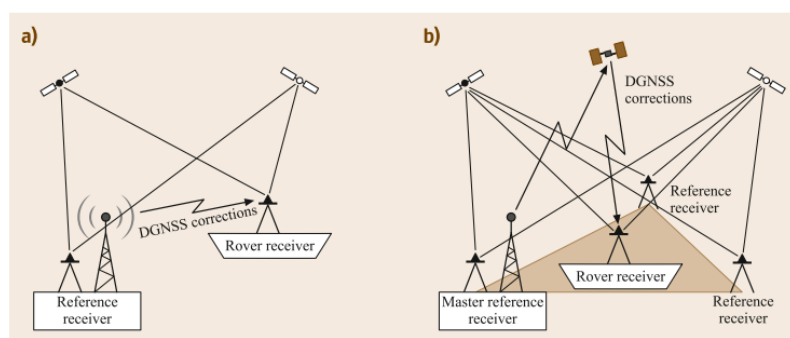


Figure 5. Working principle of (a) local DGNSS and (b) WADGNSS (P. Teunissen & Montenbruck, 2017)

Another option to process GNSS would be Precise Point Positioning (PPP) which utilizes dual-frequency, pseudorange, carrier-phase observations, and uses precise satellite orbit and

clock products to replace data from the reference station (P. Teunissen & Montenbruck, 2017). It also entails modelling of carrier-phase cycle slips as well as other environmental effects. The precise data product from the International GNSS Service (IGS) facilitates the popularity of PPP in research. For PPP, data from dual frequencies are integrated, for example in ionospheric-free (IF) combination, to significantly reduce ionospheric delay to millimetre precision. Carrier-phase observations are utilized for smoothing of the pseudo-ranges to suppress noise. Furthermore, the wet part of the tropospheric delay is expressed as a product of the mapping function and the wet zenith tropospheric delay. Other offsets need to be accounted for include the spacecraft centre of mass (CoM) and phase wind-up. Furthermore, solid earth tides are modelled by spherical harmonics expansion and physical parameters to correct the subtle deformation of the crust owing to the gravitational attraction of the sun and the moon.

i. Remote Sensing Application on ice-flow measurement

To better comprehend the physical mechanics of the Antarctica ice sheet, numerous remote sensing techniques have been utilized in research, for example, using MODIS data to study ice-sheet surface temperature variations, Landsat data to identify surface features, ASTER or TanDEM-X to extract DEM, Envisat or ICESat to investigate ice-sheet topography and GRACE to calculate ice accumulation (Quincey & Luckman, 2009). To measure tidal modulations on ice sheets, the strategies include GNSS for positioning, gravimetry for mass-change calculation, satellite altimeters for elevation measurement, and satellite synthetic aperture radar (SAR) sensor for ice-flow detection, with feature tracking technique to co-register images for retrieving the surface velocities (Gao & Liu, 2001; Padman et al., 2018; Quincey & Luckman, 2009). Many different processing strategies have been used for GNSS data processing. For instance, Lescarmonnier et al., (2012) applied both double-difference (DD) carrier phase techniques and kinematic PPP to study the vibrations of ice tongue;

whereas Horgan et al. (2013) and Wiens et al., (2008) utilize DD and differential GPS to study on-going sedimentation and tidally modulated stick-slip motion of the Whillans Ice Stream, respectively. Both Brunt, King, et al. (2010) and Brunt & MacAyeal (2014) studied the Ross Ice Shelf using PPP to detect tidal modulated ice flows. To extract tidal signals, Brunt, King, et al. (2010) fitted linear and harmonic terms in the time series at diurnal and semi-diurnal frequencies by the conventional least square method. Gudmundsson (2006), King et al. (2010), and Murray et al. (2007) also applied PPP techniques on Rutford Ice Stream, revealing the tidally induced non-linear ice-flow variations in diurnal, diurnal, two-weekly, semi-annual, and annual frequencies. The same technique has also been applied to Ronne Ice Shelf (Makinson et al., 2012; Rosier et al., 2017), Beardmore Glacier (Cooley et al., 2019) and Larsen C Ice Shelf (King, Makinson, et al., 2011; King, Padman, et al., 2011). To analyze periodic signals in GNSS data, existing toolboxes are commonly used, such as T_TIDE Matlab toolbox (eg. Padman et al., 2002) which is developed based on the FORTRAN tidal analysis package from Foreman (1977), and UTide based on MATLAB® (eg. King, Padman, et al., 2011; Rosier et al., 2017). In term of software packages, GIPSY and CSRS-PPP are the ones most extensively applied to GNSS processing and post-processing (eg. Brunt, King, et al., 2010; Lescarmonnier et al., 2012).

j. Performance deviation among GNSS strategies

The results from the available GNSS processing strategies are, however, unstandardized and hence the uncertainty shall be addressed in studies. It was found that positioning performance is influenced by GNSS scheme and processing platform. For example, Lescarmonnier et al. (2012) compared GNSS processing tools CSRS-PPP, the GINS geodetic software from CNES-GRGS and TRACK from GAMIT to assess their PPP and DD performance on detecting vibrations of the ice tongue. Results are compared on both ice and rock sites, demonstrating that GINS-PPP is superior, with RMS less than 1 cm in the horizontal

dimension and approximately 2.5 cm in the vertical dimension. Farah (2015), Martín et al. (2012), and Ozulu et al. (2018) had compared kinematic PPP results from multiple GNSS processing software packages, including CSRS-PPP, GAPS, APPS, MagicGNSS, gLAB, RTKLIB, and GrafNav. The conclusions include (1) PPP can achieve decimetres level of accuracy in general; (2) online GNSS processing services are generally more accurate compared to scientific/commercial software; (3) CSRS and magicGNSS are similarly favourable; (4) accuracy is generally higher in planimetric measurements. Although the absolute values of RMSE vary in different research papers, magicGNSS-PPP and CSRS-PPP solutions show generally RMSE less than 10 cm. The differences of accuracies between software packages can be caused by different technical specifications, as well as different performance in the modelling products. For example, research has suggested that the Zenith Tropospheric Delay (ZTD) estimation used to correct the tropospheric delay largely varies in different software packages (Mendez Astudillo et al., 2018).

III. Methodology

a. Fieldwork

During November 2018 a field program was carried out with GNSS measurements across the grounding line of Priestley Glacier, Antarctica. The length of the recorded time series in this paper is 10 days (5th to 14th November). Five geodetic L1/L2 dual-frequency GNSS-receivers (Trimble NetR9 with antenna Zephyr 3) collected observations to determine the ice movement. Two stations, Shirase and Tuati, were located upstream of the grounding line on the grounded ice, whereas the other two, Blake and Hillary, lied downstream on a free-floating ice shelf. The stations are ranging from 1 to 12 km apart. For the processing of differential GNSS, data is collected at the reference/base station on a solid rock approximately

5 km away from Hillary. Continuous observations were made every 30 seconds at Tuati and every 15 seconds at all other stations without data gaps.

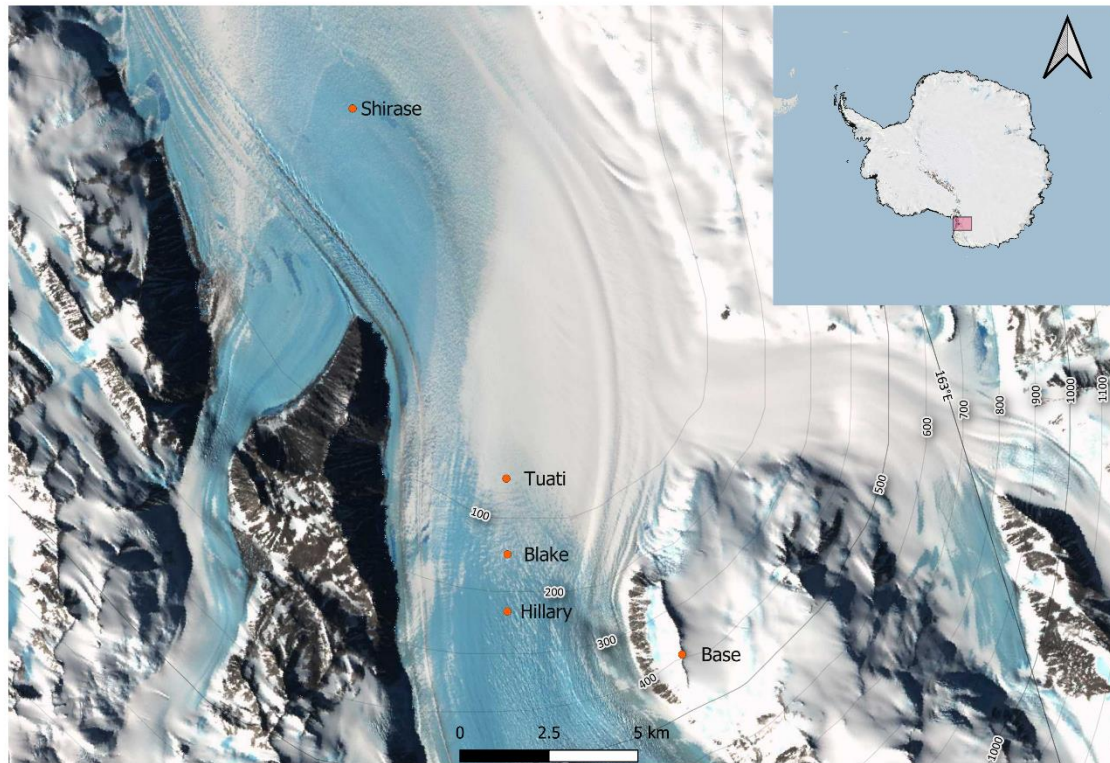


Figure 6. Map of the GNSS field stations

b. Data Processing

GNSS processing attempts were made on CSRS-PPP, gLAB-PPP, magicGNSS, RTKLIB-PPP, and RTKLIB-DGNSS, with both kinematic, dual-frequency PPP and DGNSS processing strategies as discussed above. CSRS was developed in 2003 and serves as free-of-charge online service to process RINEX data with limited customization of options (Ozulu et. al., 2018); MagicGNSS is another online free service launched in 2008, which can evaluate static and kinematic data using precise satellite orbit and clock products; gLAB was developed from the Universitat Politècnica de Catalunya (UPC) for European Space Agency (ESA) as a research and educational package for GNSS analysis of multiple processing modes; RTKLIB, on another hand, is a Japanese open source program package which allows

various processing options and detailed analysis. Except for gLAB, all solutions calculate positioning results from both GPS and GLONASS. Positioning results are obtained for all five stations in PPP, and only for moving stations in DGNSS, as the base station acts as an additional reference station for processing. No results were derived for gLAB owing to the unsupported format of input files. To process the GNSS data, the observations were sent to magicGNSS service via email and to CSRS service via its interactive webpage. The derived results and reports were retrieved shortly afterwards via email from the online services. The data was also processed in gLAB and RTKLIB on the Linux command line via a shell script. Table 2 summarizes the applied configuration options on all platforms. The processing options which cannot be customized on online services are set by default. For RTKLIB, the PPP and DGNSS options were made following the recommendations from the guidelines (Donahue et al., 2013) to achieve desired accuracies. To investigate the optimal options for RTKLIB-PPP, an experiment was carried out to examine different configuration options: those options were applied in kinematic mode on the static base station to test the stationarity of the positioning results. Details of testing options are shown in Appendix A. Results are shown to be superior with a 15-degree elevation mask, earth solid tide model, 8 filter iteration, combined modelling method and precise clock product. Also, additional testing has revealed that the differences of positioning between GPS + GLONASS and GPS is insignificant. Among all options, precise clocks are of critical importance for precise and robust positioning results, followed by combined modelling methods.

All collected results are processed in the high-level programming language Python 3.8 with Pandas Data Frame. First, the datasets were calibrated by removing the detected outliers from the daily files and performing linear interpolation for the data gaps. The high-frequency noise was removed by a Butterworth low-pass filter with cut-off frequencies determined by the Fast Fourier Transform (FFT). Additional filters were implemented on RTKLIB to reduce

the excessive spikes in solutions. Results at Tuati were removed for magicGNSS due to the system failure of kinematic processing. Secondly, mean and trend are removed from the positioning results to allow analyses of the ice-flow variations. The results were transformed into polar stereographic coordinates in metres. For the moving stations, relative distances to the base station instead of the absolute positions are calculated for simplification. Similarly, distances between base station coordinates and its position averaged over all platforms are calculated. Then moving average with a window size of 6 hours is applied before calculating horizontal and vertical velocity. Root-mean-square errors of the software are estimated from the best estimation of the base position, which is calculated by the bootstrap method with sample size 1000 over 1000 iterations. Performance analysis of the platforms is focused on ice displacement as it is directly derived/measured from GNSS data and subject to less influence by noise. It is followed by the spectral analysis which looks into the tidally modulated vertical ice displacements and horizontal ice flows.

c. Dynamic Time Warping (DTW)

Dynamic time warping (DTW) is a non-linear warping algorithm applied on two sequences to match each other: It is used to handle the distortions of time series resulting from scaling, translation, changes of shape and noise (Csillik et al., 2019; Müller, 2007). It can be carefully applied on time series to measure the fit given considerations on monotonicity, continuity, warping window, slope constraint and boundary conditions (Berndt & Clifford, 1994). As the collected GNSS data entails information of the ice flow which strongly relates to their position to the grounding line (Anandakrishnan et al., 2003; Cooley et al., 2019; Gudmundsson, 2006), DTW is performed on the solutions to calculate the minimum distance between signals at different locations. We attempt to classify locations upstream and

downstream of the grounding line respectively, which are assumed to undergo alike tidal modulations. Z-score normalization is carried out beforehand to remove the scale effect.

d. Singular Spectrum Analysis (SSA)

Singular Spectrum Analysis (SSA) is a non-parametric method which extracts information from time-domain data: it has been successfully applied to GPS time series, as well as other geodetic time series (Qiang Chen et al., 2013; Macias et al., 2014).

Although traditionally GNSS signals are usually modelled by least-square which fits harmonic terms with constant phase and amplitude, SSA shares several advantages: (1) a priori knowledge of the dynamics is not required; (2) ability to extract non-linear trend; (3) ability to extract oscillations which are amplitude and phase-modulated. It embeds a time series into an autocorrelation matrix by sliding a window, followed by applying eigenvalue decomposition and reconstruction of each identified component of the original time series using the reconstructed component series given by Vautard et al. (1992). Chen et al. (2013) assessed the performance of SSA by applying SSA, a least-square approach and a Kalman filter-based approach (Davis et al., 2012) on real GPS data from Wisconsin Point in the USA, to extract both trend and periodic oscillations. Results demonstrate that SSA and Kalman filter derived signals are statistically similar to each other and both of them perform better than LS fitting.

In the present study, SSA was implemented on the GNSS time series derived from different platforms using the pymssa package to extract periodicities of diurnal and semi-diurnal tidal frequencies. The data is first decomposed into multiple components which are later combined into independent groups according to the w-correlation matrix of components correlation. Evaluations are conducted based on the relative strengths and consistency of tidal components, as well as clear separation of noise from the signals.

Service Name	RTKLIB-DGNSS	RTKLIB-PPP	gLAB-PPP	CSRS-PPP	magicGNSS-PPP
	RTKLIB: An Open Source Program Package for GNSS Positioning	RTKLIB: An Open Source Program Package for GNSS Positioning	GNSS-Lab Tool (gLAB)	Canadian Spatial Reference System – Precise Point Positioning	magicGNSS/PPP/ Precise Point Positioning Solution
Organization & Web Page	by Tomoji TAKASU Department of Maritime Systems Engineering Tokyo University http://www.rtklib.com	by Tomoji TAKASU Department of Maritime Systems Engineering Tokyo University http://www.rtklib.com	European Space Agency (ESA) and Research group of Astronomy & Geomatics Technical University of Catalonia (gAGE/UPC) http://gage.upc.edu/gLAB	Natural Resources Canada (NRCan) http://webapp.geod.nrcan.gc.ca/geod/toolsoutils/ppp.php	GMV Innovating Solution http://magicgnss.gmv.com/ppp
Reference Frame	ITRF08	ITRF08	ITRF08	ITRF08	ITRF08
Antenna Correction	IGS	IGS	IGS	IGS	IGS
Satellite Orbits and Clocks	Center for Orbit Determination in Europe (CODE) Final	Center for Orbit Determination in Europe (CODE) Final	Center for Orbit Determination in Europe (CODE) Final	IGS Final	GMV Rapid
Elevation Mask	15°	15°	15°	7.5°	10°
GNSS System	GPS+GLONASS	GPS+GLONASS	GPS only	GPS+GLONASS	GPS+GLONASS
Used Software	RTKLib 2.4.2	RTKLib 2.4.2 GUI	gLAB_v5.4.4 Linux	CSRS_PPP	MagicGNSS (as of May 2020)
Processing Mode	Differential	Kinematic	Kinematic	Kinematic	Kinematic
Frequency processed	Dual Frequency	Dual Frequency	Dual Frequency	Dual Frequency	Dual Frequency
Observation processed	Code only	Code and Phase	Code and Phase	Code and Phase	Code and Phase
Solution Type	All epochs / Combined (Forward-Backward)	All epochs / Combined (Forward-Backward)	All epochs / Combined (Forward-Backward)	All epochs / Combined (Forward-Backward)	All epochs / Combined (Forward-Backward)
Estimation Steps	15s	15s	15s	15s	15s
Software Type	Desktop Open source Research Purpose	Desktop Open source Research Purpose	Desktop Open source Educational Purpose	Online Processing Web-based	Online Processing Web-based

Table 2. The applied strategies. The table shows the detailed processing options for GNSS schemes which have been applied in the study.

IV. Results and Discussion

a. Accuracy

From the present dataset, PPP solutions, in general, are in excellent agreement and all have achieved centimetre accuracy in the 3D space, with lower accuracy in the x-dimension. The continuous movements of stations match the flowline of the glacier and the stations flow steadily with approximate velocities of 2.8 m to 4.1 m every single day. The deviation of position is less than 5 m at the base station. The daily mean positions of all platforms are congruent, except for x positions in CSRS solutions which demonstrate a constant shift of approximate 3 to 4 m. At the base, all platforms show relatively static results, with large fluctuations on the last day of measurement. An overview of positioning solutions and the associated statistics are shown in Appendix B and C respectively. Compared to the best estimates, RMSE in the x dimension is higher for all software (Table 1). MagicGNSS reveals the most reliable and even performance in absolute positioning, closely followed by RTKLIB/PPP. CSRS demonstrates poor performance in the x dimension with RMSE over 3 m, yet exhibits exceptional accuracy in the z dimension, with an RMSE of ~7 cm. Although a shift in the scale of metres has been measured for CSRS in the x dimension, the accuracy assessment supports the previous claim that PPP strategies are generally able to achieve decimeters accuracy (Farah, 2015; Martín et al., 2012). In contrast to the previous assessment, it is shown that scientific software can achieve very comparable accuracy to online GNSS services although their precision is substandard. Also, CSRS and magicGNSS achieve similar accuracy. In contrast to the former assessment, it is noteworthy that although planimetric measurements are more accurate in RTKLIB and magicGNSS, it is the opposite in CSRS solutions, in which the z dimension appears to be the most reliable.

	RMSE (x)	RMSE (y)	RMSE (z)
CSRS/PPP	3.145	0.345	0.0665
RTKLIB/PPP	0.818	0.116	0.494
magicGNSS	0.785	0.104	0.179

Table 3. Positioning accuracy. The table displays RMSE of x, y, z from CSRS, RTKLIB, and magicGNSS solutions for PPP, expressed in metres.

b. Precision

Overall, CSRS/PPP reaches the highest precision; all PPP achieve a precision of 1 m after removal of outliers. CSRS, followed by magicGNSS, experiences less noise than RTKLIB/PPP, and performs with higher certainty. At the base, all PPP results exhibit a variance below 20 cm, whereas CSRS achieves higher than millimetre precision in all dimensions. CSRS solutions are also of leading precision at all other stations, followed by magicGNSS. In contrast, RTKLIB/PPP has a variance as high as ~7 cm in z dimension and ~1.2 m in x, y dimension. Figure 7 summarizes the overall positioning results.

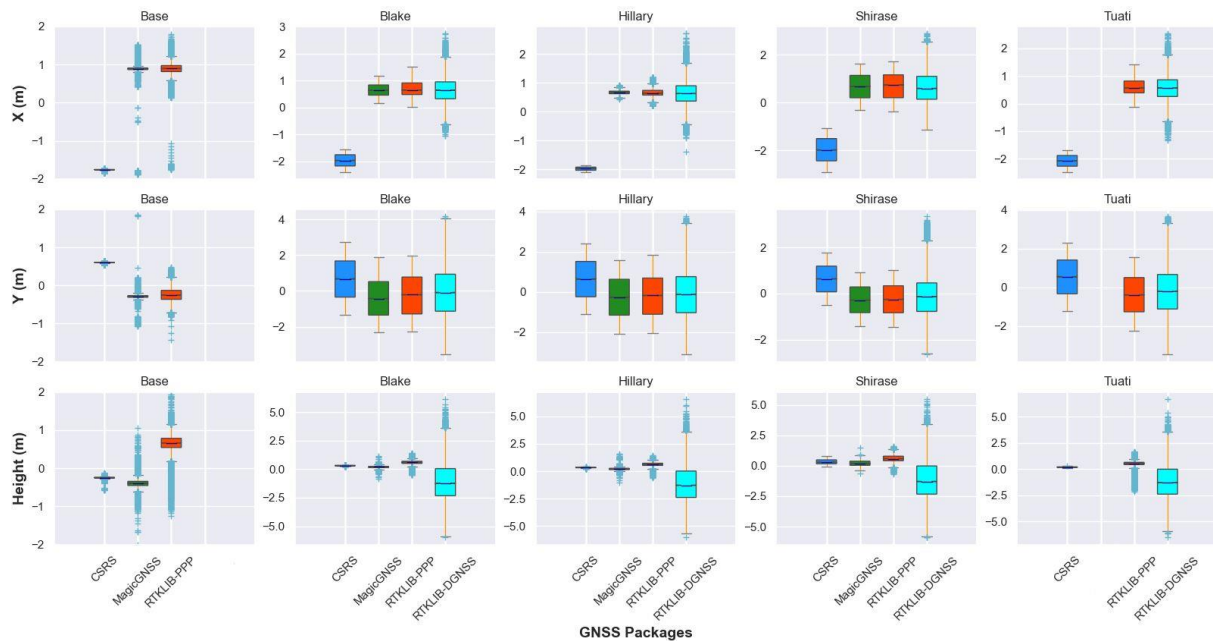


Figure 7. Positioning results. The panel shows the distributions of positions derived from CSRS/PPP (deep blue), RTKLIB/PPP (cyan), magicGNSS/PPP (green), and RTKLIB/DGNSS (orange-red) strategies, expressed in metres.

Interestingly, while most of the strategies reveal lower precision in the z dimension, CSRS demonstrates the opposite: it achieves excellent precision in height insensitive to the vertical displacement of moving stations. It can be seen, that the precision of other PPP platforms is closely correlated to the range of movement: where elevation strongly varies, such as Tuati and Shirase, the positioning results are also less precise.

Meanwhile, the precision of PPP software can be reflected by the spectrum of signals in the frequency domain. Fast Fourier Transform (FFT) converted all raw time series at the base into different frequency constituents as shown in Figure 8, displaying the amplitude versus frequency characteristics of PPP solutions. As noise refers to the ubiquitous signals with small magnitude in the periodograms, it can be seen that both magicGNSS and CSRS exhibit a clear peak and evenly distributed noise in the higher frequencies. For CSRS, the noise is generally less than 1 cm. MagicGNSS demonstrates noise of ~3 cm in solutions. In contrast, there are multiple peaks in the RTKLIB solutions, with noise possibly as large as 12 cm in uneven distribution. CSRS encapsulates the lowest signal-to-noise ratio, followed by magicGNSS. For all platforms, there are no significant deviations between noise amplitude in different dimensions. Results indicate that CSRS provides the most precise PPP solution given its small and steady noise over the frequency domain. Furthermore, as useful signals can be readily separated from noise in both CSRS and magicGNSS, noise can be better reduced from smoothing and low-pass filtering. The periodogram is thus consistent with the previous results, in which RTKLIB/PPP results demonstrate overall lowest precision. High uncertainties and noise level of RTKLIB/PPP solutions can be seen from the filtered positions, particularly at the base: large spikes frequently occur in contrast to the static position. Compared to other PPP platforms, RTKLIB solutions appear highly sensitive to the gaps where the daily files joint to produce continuous time series. Although filtering and post-processing can be implemented, the true signals will inevitably be distorted. We can therefore

conclude that for RTKLIB, the inconsistency and substandard robustness will probably limit its capacity of preserving ice motion in fine temporal resolution.

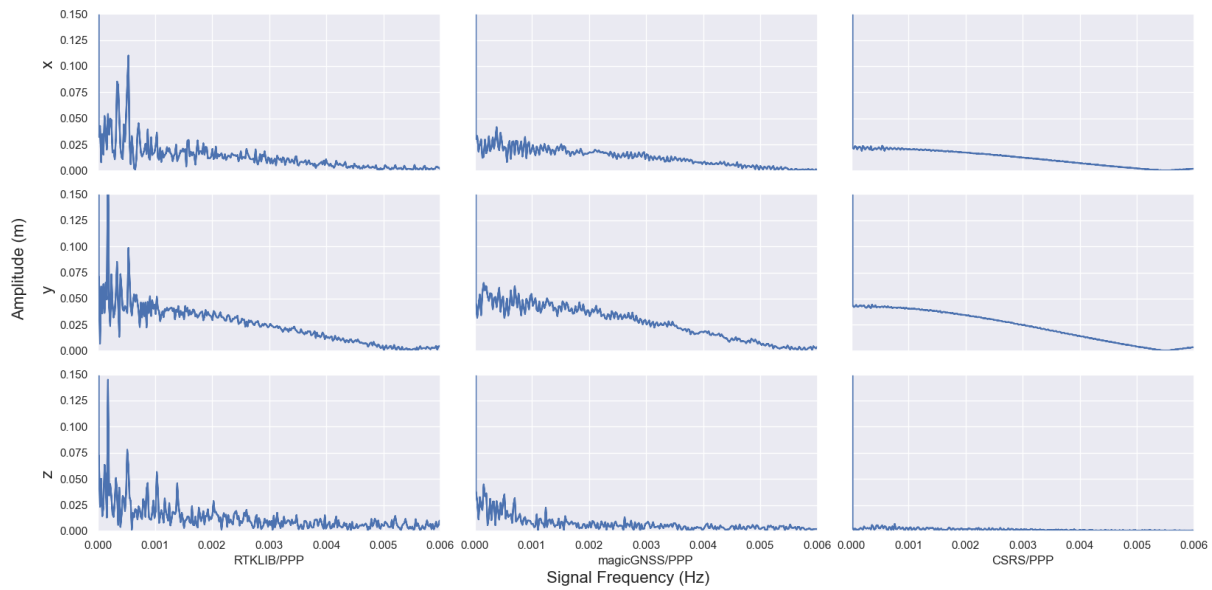


Figure 8. FFT periodogram of the frequency distribution. This figure shows spectral density of unfiltered PPP time-series in the x (top), y (middle), z (bottom) dimension using RTKLIB (left), magicGNSS (middle) and CSRS (right).

The base station is assumed to be static and its coordinates thus only constitute a distinct true value. Since all PPP solutions entail a certain amount of uncertainties in parameters measurements and atmospheric modelling for pseudorange calculation, individual mean estimates at the base do not represent its full-sample mean, but only gradually converge towards it with increasing data samples. The bootstrap method is a Monte Carlo Stimulation approach based on the given data for uncertainty calculation. It does not require assuming a parametric form for the population distribution and is robust for standard error estimation against heteroscedasticity. The plot of bootstrapping convergence (Figure 9) shows how fast the elevation estimates converge with small sample sizes: CSRS depicts merely 5 cm uncertainties in the first sample and converges very quickly to approximately 1 cm in 50 samples, whereas magicGNSS and RTKLIB depict higher uncertainties and require more samples for robust determination of positions. The first sample of magicGNSS shows

uncertainties over 30 cm within 5% confidence interval, and only converges to 1 cm in ~2000 samples; RTKLIB reveals uncertainties over 70 cm within the interval and converges to 1 cm in ~4000 samples. Furthermore, the convergence appears smoother for CSRS, which can be explained by the smaller noise and limited outliers which prevent significant interference to the useful signals. Overall, the results imply all software solutions are capable of determining static position in centimetres precision in extended time series. Comparing all PPP platforms, CSRS is the most robust as it offers precise and unequivocal results instantly even without convergence. Such implication is in line with the analyses of noise level and precision. CSRS warrants reliable performance for determining positions at the moving stations where true values vary for every timestamp: the observations are hence one-sample measurement. In this case, a robust algorithm serves to preserve kinematic positions in high temporal resolution, leading to a reliable representation of the true ice motion in terms of direction and range. It is shown in the previous analyses that, CSRS solutions are more precise than magicGNSS solutions, particular in the z dimension. This is in full support of the existing assessment study (Farah, 2015). The analysis also further reveals that CSRS solutions would achieve millimetre precision given sufficient post-processing, which is comparable to the estimations from prior studies (Farah, 2015).

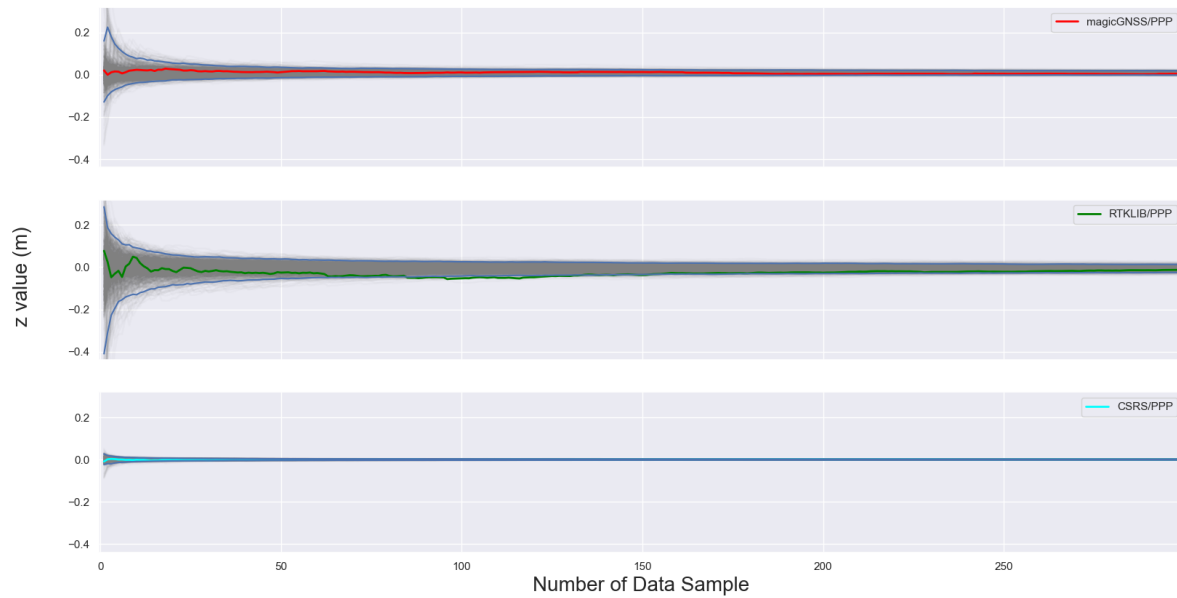


Figure 9. Bootstrapping convergence. This figure displays the convergence of independent bootstrap estimates for demeaned, detrended time series using magicGNSS/PPP (top), RTKLIB/PPP (middle) and CSRS/PPP (bottom) at the base station. The x-axis is the number of bootstrap resamples. The y-axis is the z-normalized cumulative average. It depicts the individual samplings in Monte Carlo simulation (grey), the deviations of cumulative mean from the full-sample mean (red/green/turquoise lines), and the 2.5-97.5% confidence bounds from the samples (blue line).

c. PPP versus DGNSS

RTKLIB/DGNSS (DGNSS) shows comparable accuracy yet inferior precision compared to PPP, in particular at non-static stations where noise predominates and when velocity is derived from positions. As expected, DGNSS achieves relatively low precision, showing variance from 0.18 to 0.40 m, 0.73 to 1.51 m, and over 2.5 m in the x, y, and z dimension respectively. Whilst PPP platforms show comparable ranges of estimated ice movement, DGNSS exhibits ranges twice as wide and manifests excessive outliers scattered over 10 m. Nevertheless, the DGNSS calculated positions are in good alignment with PPP at all stations. It implies that DGNSS is capable to achieve centimetre accuracy in continuous time series. The DGNSS individual measurements are, however, strongly subject to noise when applied to measure motions of the receiver. It is evident from the DGNSS height positions which exhibit strong fluctuations in the sub-daily scale compared to PPP. While PPP solutions depict spatially divergent structures in time series, DGNSS solutions oscillate every 24 hours

regardless of the location, possibly caused by noise associated with limited accuracy of the C/A code receiver with low timing precision. At Blake and Hillary where PPP solutions show no predominant oscillations, DGNSS solutions reveal a range of ~2 m, whereas at Tuati and Shirase PPP solutions exhibit daily fluctuations. Daily variations in DGNSS solutions have a decreased range of ~1.5 m and appear out of phase, which might be due to the offset against fluctuations in the ice motion. It implies that onerous post-processing is necessary when using DGNSS solutions. Nevertheless, good separation of noise is uncertain. The noise interference in DGNSS solutions is conspicuous when vertical velocity is derived from heights, in which incomprehensible periodicities of 3 hours with a range of 6 metres per hour dominate. The true patterns which entail much lower magnitude and fine structures would thus be concealed. Therefore, in comparison to PPP solutions, DGNSS appears less befitting for examining moving ice motion due to high uncertainty in kinematic measurement and restricted temporal resolution.

d. Vertical Displacement

All moving stations exhibit vertical variations over the investigated period: The patterns depend on the location, yet are also affected by the used strategies which leads to different extents of irregularity. At Tuati and Shirase, both diurnal and semi-diurnal oscillations are visible, yet the peak-to-peak amplitude and frequencies vary. DGNSS solutions are dominated by noise which impedes analyses of temporal patterns. At Blake, RTKLIB/PPP reveals periodicities every 6 hours with a range of 20 to 30 cm, whilst magicGNSS and CSRS reveal comparable patterns with more interferences and weaker signals of less than 30 and 5 cm respectively. At Hillary, the RTKLIB/PPP solution reveals a temporal pattern similar to Blake, yet with stronger non-uniformity and a range between 15 and 50 cm. Similar non-uniformity also occurs in magicGNSS and CSRS solutions. Predominant periodicities of 24 hours can be observed in both RTKLIB/PPP and CSRS solutions at Tuati and Shirase, with

higher amplitudes at Shirase and in RTKLIB solutions. All solutions are in exceptional agreement at Shirase in terms of the significant range of 50 – 75 cm, frequency and phase. It is possibly resulting from the strongest true signals at Shirase which leads to the overall highest signal-to-noise ratio. When true signals debilitate, noise becomes more salient and intervenes solutions in varying extent depending on the robustness of the algorithms: the CSRS solution is the smoothest among all solutions. Furthermore, the sensitivity of platforms to noise can be discerned from the derived vertical velocity: assuming daily height periodicities at Shirase, vertical velocity, the derivative of height differencing, is expected to peak at the steepest slope of height and arrives at troughs at the turning points. Different PPP platforms reveal different capacities to preserve such a pattern: It can barely be seen in the RTKLIB/PPP solutions but can be observed in the magicGNSS solutions despite its irregularity. In contrast, the pattern can be distinctly recognized in CSRS solutions with consistent phase and rare spikes.

e. Spatial structure of the ice motion

Supporting the foregoing analysis, DTW has revealed that the preservation of tidal frequencies in time series varies with platforms, as predominant noise will heavily disrupt temporal structure of the ice motion. In agreement with the prior studies (eg. Gudmundsson, 2006; King et al., 2010; Murray et al., 2007), Tuati and Shirase, which are located downstream of the grounding line, illustrate predominantly tidally modulated signals in both diurnal and semi-diurnal frequencies. Blake and Hillary which lie upstream of the grounding line behave correspondingly to each other, yet, do not depict mixed semi-diurnal patterns. DTW results indicate that GNSS processing strategies perform contrastingly in distinguishing the temporal patterns upstream and downstream of the grounding line. DGNSS solutions demonstrate relatively high similarities between all moving stations. It can be explained by the regular noise which dominates the time series, leading to similar oscillation patterns. In

both the magicGNSS and the RTKLIB/PPP solutions, Blake and Hillary share a relatively small minimum distance, which implies that both have captured the similarities between two time-series. RTKLIB/PPP, nevertheless, fails to distinctly assimilate tidal patterns at Shirase and Tuati, whereas CSRS solutions illustrate clear similarities between both Shirase and Tuati, and Hillary and Blake. It implicates the superior capacity of CSRS to preserve distinct characters of GNSS observation across locations, which is associated with its high signal-to-noise ratio, excellent precision, and quick convergence of positions. The current analysis points out that (1) DGNSS solutions are relatively predominated by noise; (2) CSRS can best preserve the sub-daily tidal modulations in 1D time series. We can therefore conclude, that in line with the preceding precision evaluation, CSRS demonstrates high robustness against noise and is preferable to examine the fine temporal structures of kinematic GNSS observations.

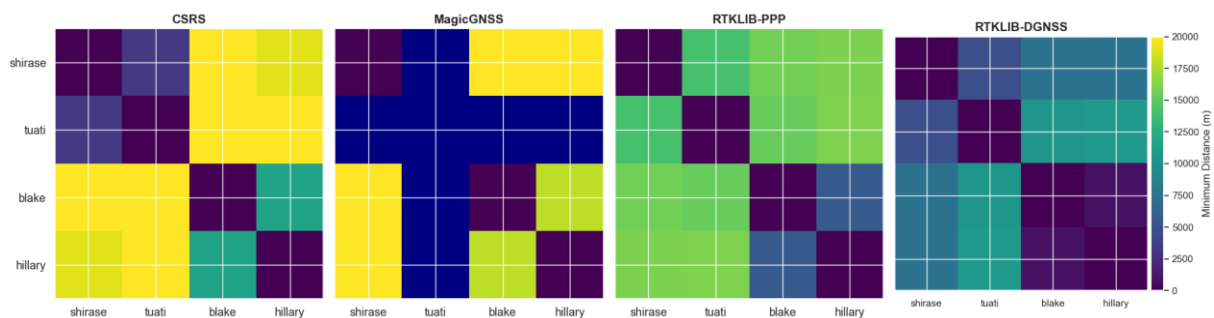


Figure 10. The similarity of the time series. This figure illustrates the similarity between positioning solutions using CSRS/PPP, magicGNSS/PPP, and RTKLIB/PPP. The value bar refers to the estimated minimum distance from DTW. The dark blue colour in magicGNSS refers to bad values.

Apart from the inter-station comparison, the spectral estimation method has manifested the critical importance of signal strength in tidal frequencies on the consistent performance of GNSS solutions: competent preservation of tidal modulations in centimetres range demands excellent precision in kinematic positioning. From the SSA results, we can investigate further into the decomposition of oscillatory components in signal reconstruction. By knowing the frequencies of ocean tides, tidal signals can be extracted by SSA in varying extents depending

on the noise and signal completeness in the observations. Overall, the tidal modulations at Shirase are the most distinct: it can be readily decomposed into predominant signals at diurnal and semi-diurnal periods in the CSRS and magicGNSS solutions, explaining 70% and 15% of the variance using CSRS, and 75% and 20% using magicGNSS. Yet, CSRS allows a more complete reconstruction. In RTKLIB/PPP solutions, noise occupies 5 to 10% of the variance and solely diurnal signals can be decomposed. At Tuati, the CSRS solution allows the reconstruction of diurnal and semi-diurnal signals, with magnitudes reduced by approximately 90%, whereas only 24-hours signals can be extracted from the RTKLIB/PPP solution. At Hillary and Blake, whilst CSRS solution allows the extraction of semi-diurnal signals less than 4 cm and 2 cm individually, RTKLIB/PPP and magicGNSS solutions do not allow meaningful reconstruction at the tidal frequencies.

Overall, the SSA results are very compatible with DTW results, in which time series from Tuati and Shirase are alike as they both share oscillations in diurnal and semi-diurnal frequencies. Although the satisfactory reconstruction can be performed at Shirase and Tuati regardless of platforms, constructive decomposition at Blake and Hillary is only allowed using CSRS with PPP. It is possibly due to the weak tidal modulation, i.e. ranging from 2 to 4 cm, which is prone to be covered up by the high-frequency noise. As analysis has shown that CSRS allows millimetre precision which is beyond 10 times more precise compared to other solutions, it is unsurprising that solely CSRS can well preserve tidal modulations in centimetres range. According to the SSA results, it is evident that the adaptation of different GNSS platforms will strongly alter the results in tidal analysis. The inadequate robustness of processing strategies will deteriorate the solutions, shown by the reduced magnitude and high variance of target signals in time series. With the present dataset, consistent performance of the platforms begins to deviate once the tidal constituents drop below decimeters level. The reduced performance is strongly associated with the insufficient precision of position

measurement. Based on the SSA analysis, CSRS provides an optimal solution which is sufficiently robust to capture the mixed semi-diurnal tidal patterns in the modulated ice motion. CSRS is, hence, used for further tidal analysis.

f. Observations of Tidal Modulation

In CSRS solutions, tidally modulated signals are discernible in both vertical displacement and horizontal velocity: They are the most significant near the marine margin and grounding line, respectively. The fine preservation of tidal signals in the centimetre range is indicative of the robust and precise performance of the CSRS and the PPP strategy. Figure 11 shows the tidal analysis results concerning vertical positions along the flowline. The measured tides in the Ross Sea are mixed semi-diurnal. Overall, observed vertical variations across stations are in agreement with the tidal range. Notwithstanding, tidal modulations are stronger on floating ice shelf than on grounded ice. It has been revealed that the height oscillations in tidal frequencies shown in SSA are clearly associated with tidal perturbations. At the ice front, Shirase demonstrates diurnal signals comparable or even beyond the tidal range with less than 20 cm deviations over 10 days. The signals are also in phase with the tides. Meantime, Tuati which locates just downstream of the grounding line manifests in largely reduced in-phase tidal signals: Its range has dropped from 20 - 50 cm to ~5 cm. Opposed to observations on the ice shelf, diurnal modulations are not depicted upstream of the grounding line where the vertical displacements are also the weakest. On another hand, clear evidence of tidally modulated horizontal ice-flow velocity has been shown using CSRS solutions. The modulations amplify when it approaches the grounding line: After removing the mean, horizontal velocities at Tuati reveals diurnal oscillations of ~5 mm/day with 90-degree phase difference with ocean tides. At Blake, the range is 0.9 mm/day with the same phase. It is worth noting that, at Shirase, tidally modulated horizontal velocity is slightly recognizable, nonetheless, shows no phase shift to the tides. Hillary shows unclear variations to both diurnal

and semi-diurnal tidal frequencies. The SSA reconstruction of time series at all moving station is shown in Appendix D.

A comparison of local tides and vertical variations in Figure 11 suggests a correlation between tidally modulated vertical deflection and distance to the ice front, whereas the spatial variations in horizontal velocities in Figure 12 propound the importance of ice flow dynamics at the grounding line. It indicates that the perturbations of tides in the Ross Sea have altered the ice-shelf and grounded-ice responses over the extensive distance between the grounding zone and marine margin. This implication on divergent spatial structures of tidal modulation is generally in good agreement with the literature and has provided supportive evidence of GNSS observations on Priestley Glacier across the grounding line. Despite the long-term tidal cycle being not considered in the present study, the detected diurnal and semi-diurnal oscillations in the sub-daily scale match the previous observations concerning both vertical deflections and horizontal velocity. Similar to the previous records at Nascent Iceberg on Ross Ice Shelf (Brunt, Fricker, et al., 2010), GNSS stations on the ice shelf demonstrate strongly modified ice-flow patterns at the tidal frequencies. The tidally modulated behaviours of the Ross Ice Shelf from the recorded GNSS observations over 10 days are also comparable to Larsen C Ice Shelf and Ronne Ice Shelf in Antarctica (King et al., 2011; Makinson et al., 2012). As suggested by fieldwork at Beardmore Glacier, the present study supports the largest horizontal flow near the grounding line and its gradual decreases downstream (Cooley et al., 2019). The tidally induced vertical deflections which are detected on grounded ice also correspond to the former observations at the grounding zone of Ekströmisen (Riedel et al., 1999). The latest data set collected on Priestley Glacier, along with the prior studies, has thereby, underpinned the complex interplay between buttressing from the free-floating ice shelf, the local ocean tides, and the ice flow near the grounding line.

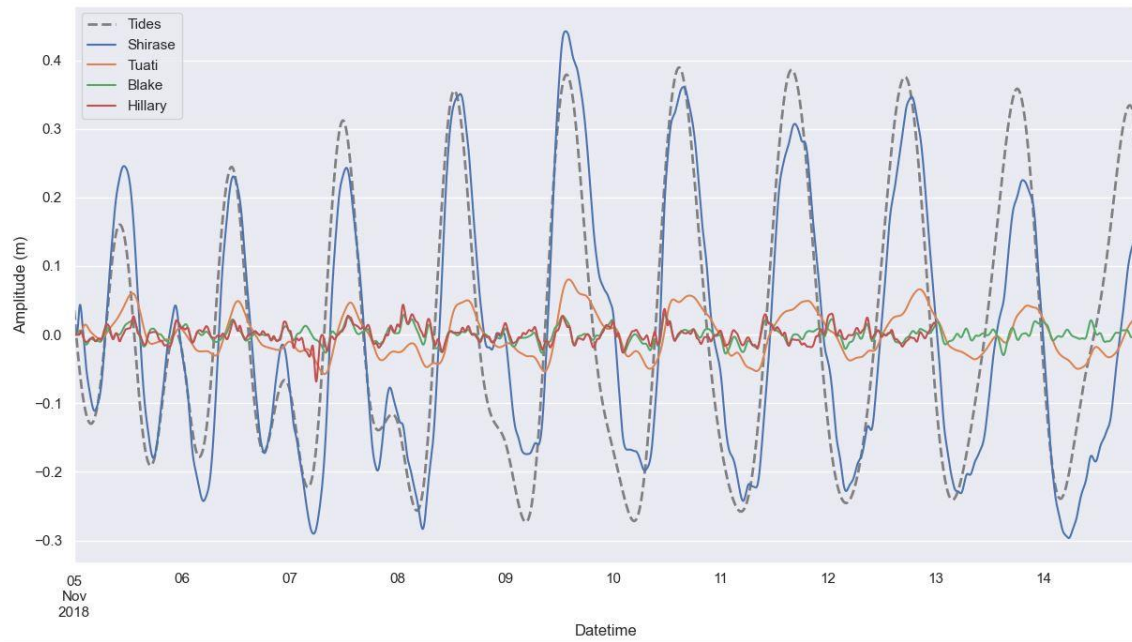


Figure 11. Vertical variations. The panel shows vertical displacements over 10 days on grounded ice and ice shelf at the grounding zone: Shirase (blue), Tuati (orange), Hillary (red), Blake (green) and local tides (grey dash line).

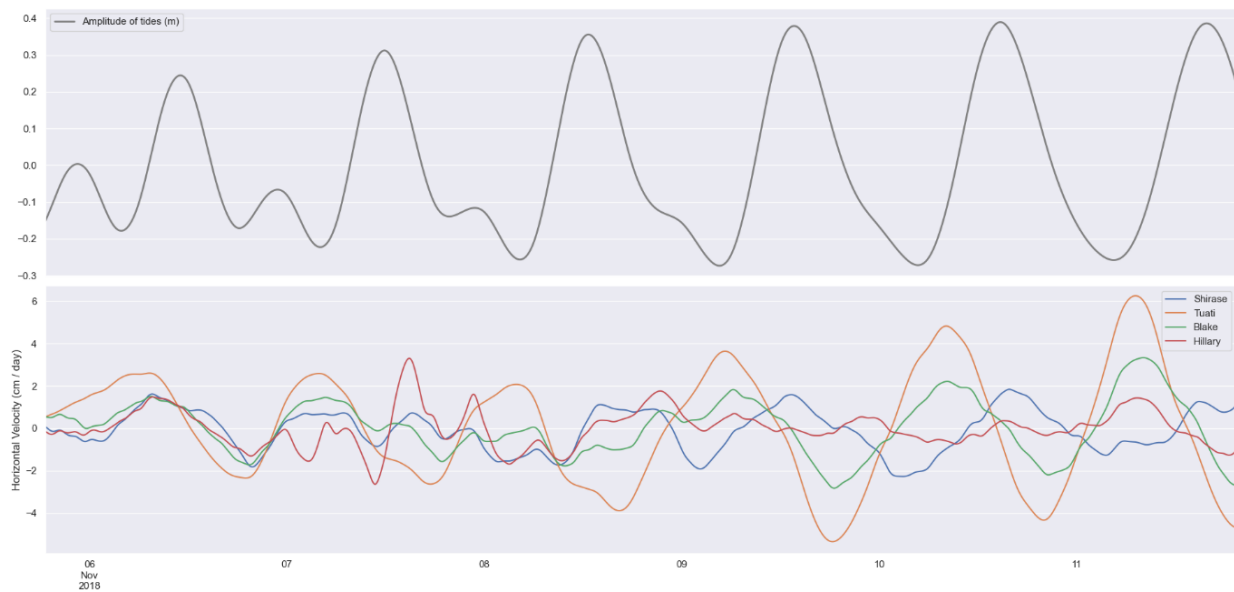


Figure 12. Horizontal velocities. This figure illustrates the demean horizontal velocities in millimetres per day (bottom panel) over 6 days (06 - 11 November 2018) at Shirase (blue), Tuati (orange), Blake (green) and Hillary (red) along with the local tidal ranges (upper panel).

To summarize, DGNSS are able to reach decimeter accuracy for the static position.

Nevertheless, DGNSS solutions are the noisiest and imprecise ones which lead to frail solutions when used to detect oscillating ice positions. PPP solutions, in general, can achieve

better precision and have good capacity to detect temporal patterns in sub-daily scale with a decimeter range. MagicGNSS is highly competent overall. Its solution is highly accurate in all dimension with no significant shift. It is distinctly precise and shows limited noise after filtering, however, its performance declines when tidal signals drop below decimeters range. Whilst magicGNSS can preserve tidal modulations at Tuati and Shirase, the tidal signals become marginal at Blake and Hillary. CSRS is inaccurate in planimetric measurements compared to other platforms. It achieves, however, excellent accuracy in the z dimension. It is the most precise among all platforms with a variance below 1 cm. It is demonstrated in the spectral analysis that CSRS is capable of preserving tidal signals of less than 5 centimetres, which is superior compared to other strategies. Other noteworthy empirical aspects include: (1) magicGNSS is mail-based which limits the size of the input RINEX file to 20 MB, (2) RTKLIB offers a full range of customizable options compared to magicGNSS and CSRS, and (3) magicGNSS has demonstrated an internal failure of kinematic positioning.

Furthermore, some limitations should be noted in the present assessment. First, the accuracy in positioning is based on best estimates from the bootstrap method as the base station is not an official geodetic point and subject to systematic biases. The data set is sampled for a short period so the ranges and temporal patterns are not fully representative on a larger scale.

Secondly, long term tidal signals are not considered in this study. It implies, that the spectral analysis of solutions are incomplete as the long term signals are overlooked and treated as noise or residuals. Moreover, the settings in different processing schemes are unidentical which might lead to a bias in the comparison. As the DGNSS solutions have been only processed with RTKLIB, the results might not represent other DGNSS processing platforms. Nonetheless, the conclusion is illustrative since the deviation of performance between PPP and DGNSS are significant and align with current knowledge. Finally, the analysis of carrier-

phase based DGNSS, which is superior to code-based DGNSS, is not included in the current study due to the limited availability of processing platforms.

V. Conclusion

This research presented an evaluation study for the reliability of kinematic GNSS positioning in the tidal analysis based on different GNSS kinematic processing schemes (PPP and DGNSS) and post-processing software packages. It is to better understand the role of GNSS post-processing options on extracting sub-daily tidal modulations from 1D time series in high temporal resolutions. Based on the existing literature, it is expected that PPP outperforms DGNSS, and online-GNSS services achieve higher performance than the academic software. Assessment is performed based on precision, accuracy using the bootstrap approach, and preservation of tidal modulation in temporal analysis, which applies dynamic time warping for inter-station comparison and singular spectral analysis for tidal decomposition in the frequency domain. The results are generally in line with the expectations: The choice of platform and processing schemes do impose significant differences in solutions. Online GNSS services including CSRS and magicGNSS, are preferred over RTKLIB. It is, however, found that DGNSS, despite its low precision, is able to achieve comparable accuracy.

The present work highlights how the adaptation of platforms with low precision can obstruct the extraction of centimetre-scale tidal modulation. It has been shown in general that both DGNSS and PPP can determine static positions in decimeter accuracy, yet only PPP can achieve centimetre and even millimetre precision. Capacity to achieve high precision can significantly boost the performance in tidal analysis in which diurnal and semi-diurnal modulations can drop below four centimetres. A successful tidal analysis is shown to be best achieved by CSRS/PPP among all adapted GNSS strategies. CSRS has reached variance below five millimetres in the current study and performs exceptionally in elevation measurements. Its standard error in the z dimension stays below seven centimetres, which

warrants the preservation of vertical ice motion. Among all raw solutions, CSRS has the highest signal-to-noise ratio. Besides, it is the fastest to converge which is evidently advantageous for detecting ice movement where multiple samples are unavailable. According to results from dynamic time warping, stations located upstream and downstream of the grounding line have shown clear structural differences in the vertical ice motion despite both groups depict clear tidal modulations to varying extents. In general, PPP can effectively detect the deviations of ice motions, while only CSRS/PPP has successfully distinguished different moving patterns among all stations. Consistent implications can be made from SSA results, although the performance is also highly dependent on the signal strengths. Although all PPP solutions have revealed diurnal and semi-diurnal tidal signals in Shirase and Tuati, only CSRS/PPP has revealed semi-diurnal signals at Blake and Hillary. In addition to these findings, the study presents the successful application of singular spectrum analysis to study GNSS kinematic time series in the Antarctic context. It is evident that, instead of conventionally used least-square approach, SSA, which allows the simple use of an existing implementation in Python, is highly effective to decompose tidal modulations in ice motion into multiple individual frequencies.

By looking further into the signals in different tidal frequencies, both Tuati and Shirase have shown diurnal and semi-diurnal signals in the vertical displacements. Whilst diurnal signals cannot be observed in Hillary and Blake, semi-diurnal signals are still recognizable, with a range of several centimetres. All tidal modulations are in phase with the local tides in the Ross Sea. The horizontal velocity is tidally modulated with different patterns across the grounding zone. The tidal modulation amplifies with decreasing distance to the grounding line and demonstrates a 90-degree phase difference to the tides except for Shirase which exhibits in-phase oscillations. Tuati depicts the highest variations, oscillating at maximum 10 cm per day. Blake and Shirase, on the other hand, show only half of the variations. At low

tides, the horizontal ice flow reaches its troughs at Shirase, and peaks at Tuati as well as Blake. The observations of the surface motion of the Priestley Glacier indicate a strong and non-uniform response that propagates both upstream and downstream of the grounding line, and meanwhile, intervenes with the vertical deflection of the free-floating ice shelf. It implicates temporal patterns in both elevation and horizontal ice flow are associated with the tidal modulation, yet entail different sets of processes in ice dynamics, leading to distinct responses at different GNSS stations. Its spatial variations offer an insight into the physical mechanism taking place at the grounding zone. Further investigating the distinct tidally modulated patterns upstream of the grounding line can facilitate understandings of the corresponding ice dynamics. Quantifying this complex interplay between grounding line, ice flow motion, and ocean tides require further observations and modelling efforts.

REFERENCES

- Anandakrishnan, S., Voigt, D. E., Alley, R. B., & King, M. A. (2003). Ice stream D flow speed is strongly modulated by the tide beneath the Ross Ice Shelf. *Geophysical Research Letters*, 30(7). <https://doi.org/10.1029/2002GL016329>
- Baumhoer, C. A., Dietz, A. J., Dech, S., & Kuenzer, C. (2018). Remote sensing of antarctic glacier and ice-shelf front dynamics—A review. *Remote Sensing*, 10(9), 1445.
- Begeman, C. B., Tulaczyk, S., Padman, L., King, M., Siegfried, M. R., Hodson, T. O., & Fricker, H. A. (2020). Tidal Pressurization of the Ocean Cavity Near an Antarctic Ice Shelf Grounding Line. *Journal of Geophysical Research: Oceans*, 125(4). <https://doi.org/10.1029/2019JC015562>
- Berndt, D. J., & Clifford, J. (1994, July). *Using dynamic time warping to find patterns in time series*. In KDD workshop (Vol. 10, No. 16, pp. 359-370).
- Bindschadler, R. A., King, M. A., Alley, R. B., Anandakrishnan, S., & Padman, L. (2003). *Tidally Controlled Stick-Slip Discharge of a West Antarctic Ice Stream*. 301, 3.
- Brenner, A. C., DiMarzio, J. P., & Zwally, H. J. (2007). Precision and Accuracy of Satellite Radar and Laser Altimeter Data Over the Continental Ice Sheets. *IEEE Transactions on Geoscience and Remote Sensing*, 45(2), 321–331. <https://doi.org/10.1109/TGRS.2006.887172>
- Brunt, K. M., Fricker, H. A., & Padman, L. (2011). Analysis of ice plains of the Filchner–Ronne Ice Shelf, Antarctica, using ICESat laser altimetry. *Journal of Glaciology*, 57(205), 965–975. <https://doi.org/10.3189/002214311798043753>
- Brunt, K. M., Fricker, H. A., Padman, L., Scambos, T. A., & O’Neel, S. (2010). Mapping the grounding zone of the Ross Ice Shelf, Antarctica, using ICESat laser altimetry. *Annals of Glaciology*, 51(55), 71–79. <https://doi.org/10.3189/172756410791392790>

- Brunt, K. M., King, M. A., Fricker, H. A., & MacAyeal, D. R. (2010). Flow of the Ross Ice Shelf, Antarctica, is modulated by the ocean tide. *Journal of Glaciology*, 56(195), 157–161. <https://doi.org/10.3189/002214310791190875>
- Brunt, K. M., & MacAyeal, D. R. (2014). Tidal modulation of ice-shelf flow: A viscous model of the Ross Ice Shelf. *Journal of Glaciology*, 60(221), 500–508. <https://doi.org/10.3189/2014JoG13J203>
- Chen, Q., Weigelt, M., Sneeuw, N., & van Dam, T. (2015). On time-variable seasonal signals: Comparison of SSA and Kalman filtering based approach. *VIII Hotine-Marussi Symposium on Mathematical Geodesy*, 75–80.
- Chen, Qiang, van Dam, T., Sneeuw, N., Collilieux, X., Weigelt, M., & Rebischung, P. (2013). Singular spectrum analysis for modeling seasonal signals from GPS time series. *Journal of Geodynamics*, 72, 25–35.
- Church, J. A., Clark, P. U., Cazenave, A., Gregory, J. M., Jevrejeva, S., Levermann, A., ... & Payne, A. J. (2013). *Sea level change*. PM Cambridge University Press.
- Cooley, J., Winberry, P., Koutnik, M., & Conway, H. (2019). Tidal and spatial variability of flow speed and seismicity near the grounding zone of Beardmore Glacier, Antarctica. *Annals of Glaciology*, 60(79), 37–44. <https://doi.org/10.1017/aog.2019.14>
- Csillik, O., Belgiu, M., Asner, G. P., & Kelly, M. (2019). Object-based time-constrained dynamic time warping classification of crops using Sentinel-2. *Remote Sensing*, 11(10), 1257.
- Cuffey, K. M., & Paterson, W. S. B. (2010). *The Physics of Glaciers*. Academic Press.
- Davis, J. L., Wernicke, B. P., & Tamisiea, M. E. (2012). On seasonal signals in geodetic time series. *Journal of Geophysical Research: Solid Earth*, 117(B1).
- Dawoud, S. (2012). *GNSS principles and comparison*. Potsdam University.

- Donahue, B., Surveyor General Branch, Wentzel, J., & Berg, R. (2013). *Guidelines for RTK/RTN GNSS surveying in Canada* (No. 100E; p. 100E).
<https://doi.org/10.4095/292856>
- Dupont, T. K., & Alley, R. B. (2005). Assessment of the importance of ice-shelf buttressing to ice-sheet flow. *Geophysical Research Letters*, 32(4).
<https://doi.org/10.1029/2004GL022024>
- Farah, A. (2015). Accuracy Assessment Study for Kinematic GPS–PPP Using Single- and Dual-Frequency Observations with Various Software Packages. *Arabian Journal for Science and Engineering*, 40(7), 2013–2019. <https://doi.org/10.1007/s13369-015-1613-1>
- Foreman, M. G. G. (1977). Manual for Tidal Heights Analysis and Prediction. Pacific Marine Science Report. 77–10. Institute of Ocean Sciences, Patricia Bay, 58 pp. *British Columbia, Canada*.
- Fricker, H. A., Coleman, R., Padman, L., Scambos, T. A., Bohlander, J., & Brunt, K. M. (2009). Mapping the grounding zone of the Amery Ice Shelf, East Antarctica using InSAR, MODIS and ICESat. *Antarctic Science*, 21(5), 515–532.
<https://doi.org/10.1017/S095410200999023X>
- Gao, J., & Liu, Y. (2001). Applications of remote sensing, GIS and GPS in glaciology: a review. *Progress in Physical Geography*, 25(4), 520–540.
- Goldberg, D. N. (2016). Ice shelf buttressing. *International Encyclopedia of Geography: People, the Earth, Environment and Technology: People, the Earth, Environment and Technology*, 1–9.
- Gudmundsson, G. H. (2011). Ice-stream response to ocean tides and the form of the basal sliding law. *The Cryosphere*, 5(1), 259–270. <https://doi.org/10.5194/tc-5-259-2011>

- Gudmundsson, G. Hilmar. (2006). Fortnightly variations in the flow velocity of Rutford Ice Stream, West Antarctica. *Nature*, 444(7122), 1063–1064.
<https://doi.org/10.1038/nature05430>
- Haseloff, M., & Sergienko, O. V. (2018). The effect of buttressing on grounding line dynamics. *Journal of Glaciology*, 64(245), 417–431.
<https://doi.org/10.1017/jog.2018.30>
- He, K. (2015). GNSS kinematic position and velocity determination for airborne gravimetry. *Scientific Technical Report; 15/04*. <https://doi.org/10.2312/GFZ.B103-15044>
- Horgan, H. J., Christianson, K., Jacobel, R. W., Anandakrishnan, S., & Alley, R. B. (2013). Sediment deposition at the modern grounding zone of Whillans Ice Stream, West Antarctica. *Geophysical Research Letters*, 40(15), 3934–3939.
<https://doi.org/10.1002/grl.50712>
- Joughin, I., & Alley, R. B. (2011). Stability of the West Antarctic ice sheet in a warming world. *Nature Geoscience*, 4(8), 506–513. <https://doi.org/10.1038/ngeo1194>
- King, M. A., Makinson, K., & Gudmundsson, G. H. (2011). Nonlinear interaction between ocean tides and the Larsen C Ice Shelf system. *Geophysical Research Letters*, 38(8).
<https://doi.org/10.1029/2011GL046680>
- King, M. A., Murray, T., & Smith, A. M. (2010). Non-linear responses of Rutford Ice Stream, Antarctica, to semi-diurnal and diurnal tidal forcing. *Journal of Glaciology*, 56(195), 167–176. <https://doi.org/10.3189/002214310791190848>
- King, M. A., Padman, L., Nicholls, K., Clarke, P. J., Gudmundsson, G. H., Kulesa, B., & Shepherd, A. (2011). Ocean tides in the Weddell Sea: New observations on the Filchner-Ronne and Larsen C ice shelves and model validation. *Journal of Geophysical Research: Oceans*, 116(C6). <https://doi.org/10.1029/2011JC006949>

- Langley, R. B., Teunissen, P. J. G., & Montenbruck, O. (2017). Introduction to GNSS. In P. J. G. Teunissen & O. Montenbruck (Eds.), *Springer Handbook of Global Navigation Satellite Systems* (pp. 3–23). Springer International Publishing.
https://doi.org/10.1007/978-3-319-42928-1_1
- Lescarmonier, L., Legrésy, B., Coleman, R., Perosanz, F., Mayet, C., & Testut, L. (2012). Vibrations of Mertz Glacier ice tongue, East Antarctica. *Journal of Glaciology*, 58(210), 665–676. <https://doi.org/10.3189/2012JoG11J089>
- Macias, D., Stips, A., & Garcia-Gorritz, E. (2014). Application of the singular spectrum analysis technique to study the recent hiatus on the global surface temperature record. *PLoS One*, 9(9), e107222.
- Makinson, K., King, M. A., Nicholls, K. W., & Gudmundsson, G. H. (2012). Diurnal and semidiurnal tide-induced lateral movement of Ronne Ice Shelf, Antarctica. *Geophysical Research Letters*, 39(10). <https://doi.org/10.1029/2012GL051636>
- Martín, A., Anquela, A. B., Berné, J. L., & Sanmartin, M. (2012). Kinematic GNSS-PPP results from various software packages and raw data configurations. *Scientific Research and essays*, 7(3), 419–431.
- Mendez Astudillo, J., Lau, L., Tang, Y.-T., & Moore, T. (2018). Analysing the zenith tropospheric delay estimates in on-line precise point positioning (PPP) services and PPP software packages. *Sensors*, 18(2), 580.
- Müller, M. (Ed.). (2007). Dynamic Time Warping. In *Information Retrieval for Music and Motion* (pp. 69–84). Springer. https://doi.org/10.1007/978-3-540-74048-3_4
- Murray, T., Smith, A. M., King, M. A., & Weedon, G. P. (2007). Ice flow modulated by tides at up to annual periods at Rutford Ice Stream, West Antarctica. *Geophysical Research Letters*, 34(18). <https://doi.org/10.1029/2007GL031207>

- Padman, L., Fricker, H. A., Coleman, R., Howard, S., & Erofeeva, L. (2002). A new tide model for the Antarctic ice shelves and seas. *Annals of Glaciology*, 34, 247–254.
<https://doi.org/10.3189/172756402781817752>
- Padman, L., Siegfried, M. R., & Fricker, H. A. (2018). Ocean Tide Influences on the Antarctic and Greenland Ice Sheets. *Reviews of Geophysics*, 56(1), 142–184.
<https://doi.org/10.1002/2016RG000546>
- Ozulu, I. M., ilçi, V., Erol, S., & Alkan, R. (2018). *Kinematic PPP Positioning Using Different Processing Platforms*. FIG Congress, Istanbul, Turkey.
https://www.researchgate.net/publication/331555574_Kinematic_PPP_Positioning_Using_Different_Processing_Platforms
- Pieraccini, M., & Miccinesi, L. (2019). Ground-based radar interferometry: A bibliographic review. *Remote Sensing*, 11(9), 1029.
- Priestley Glacier*. (2012). Antarctica NZ. Retrieved September 16, 2020, from
<https://adam.antarcticanz.govt.nz/nodes/view/21635>
- Pritchard, H. D., Ligtenberg, S. R. M., Fricker, H. A., Vaughan, D. G., van den Broeke, M. R., & Padman, L. (2012). Antarctic ice-sheet loss driven by basal melting of ice shelves. *Nature*, 484(7395), 502–505. <https://doi.org/10.1038/nature10968>
- Quincey, D. J., & Luckman, A. (2009). Progress in satellite remote sensing of ice sheets. *Progress in Physical Geography*, 33(4), 547–567.
- Reeh, N., Christensen, E. L., Mayer, C., & Olesen, O. B. (2003). Tidal bending of glaciers: A linear viscoelastic approach. *Annals of Glaciology*, 37, 83–89.
<https://doi.org/10.3189/172756403781815663>
- Rémy, F., & Frezzotti, M. (2006). Antarctica ice sheet mass balance. *Comptes Rendus Geoscience*, 338(14–15), 1084–1097.

- Riedel, B., Nixdorf, U., Heinert, M., Eckstaller, A., & Mayer, C. (1999). The response of the Ekströmsisen (Antarctica) grounding zone to tidal forcing. *Annals of Glaciology*, 29, 239–242. <https://doi.org/10.3189/172756499781821247>
- Rignot, E., Mouginot, J., & Scheuchl, B. (2011). Ice Flow of the Antarctic Ice Sheet. *Science*, 333(6048), 1427–1430. <https://doi.org/10.1126/science.1208336>
- Rignot, Eric. (1998). Radar interferometry detection of hinge-line migration on Rutford Ice Stream and Carlson Inlet, Antarctica. *Annals of Glaciology*, 27, 25–32. <https://doi.org/10.3189/1998AoG27-1-25-32>
- Robel, A. A., Tsai, V. C., Minchew, B., & Simons, M. (2017). Tidal modulation of ice shelf buttressing stresses. *Annals of Glaciology*, 58(74), 12–20. <https://doi.org/10.1017/aog.2017.22>
- Rosier, S. H. R., Gudmundsson, G. H., & Green, J. A. M. (2014). Insights into ice stream dynamics through modelling their response to tidal forcing. *The Cryosphere*, 8(5), 1763–1775. <https://doi.org/10.5194/tc-8-1763-2014>
- Rosier, S. H. R., Gudmundsson, G. H., & Green, J. A. M. (2015). Temporal variations in the flow of a large Antarctic ice stream controlled by tidally induced changes in the subglacial water system. *The Cryosphere*, 9(4), 1649–1661. <https://doi.org/10.5194/tc-9-1649-2015>
- Rosier, Sebastian H. R., & Gudmundsson, G. H. (2016). Tidal controls on the flow of ice streams. *Geophysical Research Letters*, 43(9), 4433–4440. <https://doi.org/10.1002/2016GL068220>
- Rosier, S., Gudmundsson, H., King, M., Nicholls, K., Makinson, K., & Corr, H. (2017). Strong tidal variations in ice flow observed across the entire Ronne Ice Shelf and adjoining ice streams. *Earth System Science Data*, 9, 849–860.

- Siegfried, M. R., Fricker, H. A., Carter, S. P., & Tulaczyk, S. (2016). Episodic ice velocity fluctuations triggered by a subglacial flood in West Antarctica. *Geophysical Research Letters*, 43(6), 2640–2648. <https://doi.org/10.1002/2016GL067758>
- Teunissen, P., & Montenbruck, O. (2017). *Springer Handbook of Global Navigation Satellite Systems*. Springer.
- Thomas, R. H. (1985). *Satellite remote sensing for ice sheet research*.
- Tsai, V. C., & Gudmundsson, G. H. (2015). An improved model for tidally modulated grounding-line migration. *Journal of Glaciology*, 61(226), 216–222. <https://doi.org/10.3189/2015JoG14J152>
- Vautard, R., Yiou, P., & Ghil, M. (1992). Singular-spectrum analysis: A toolkit for short, noisy chaotic signals. *Physica D: Nonlinear Phenomena*, 58(1–4), 95–126.
- Walker, R. T., Christianson, K., Parizek, B. R., Anandakrishnan, S., & Alley, R. B. (2012). A viscoelastic flowline model applied to tidal forcing of Bindschadler Ice Stream, West Antarctica. *Earth and Planetary Science Letters*, 319–320, 128–132. <https://doi.org/10.1016/j.epsl.2011.12.019>
- Walker, R. T., Parizek, B. R., Alley, R. B., Anandakrishnan, S., Riverman, K. L., & Christianson, K. (2013). Ice-shelf tidal flexure and subglacial pressure variations. *Earth and Planetary Science Letters*, 361, 422–428. <https://doi.org/10.1016/j.epsl.2012.11.008>
- Walker, R. T., Parizek, B. R., Alley, R. B., Brunt, K. M., & Anandakrishnan, S. (2014). Ice-shelf flexure and tidal forcing of Bindschadler Ice Stream, West Antarctica. *Earth and Planetary Science Letters*, 395, 184–193. <https://doi.org/10.1016/j.epsl.2014.03.049>
- Wiens, D. A., Anandakrishnan, S., Winberry, J. P., & King, M. A. (2008). Simultaneous teleseismic and geodetic observations of the stick–slip motion of an Antarctic ice stream. *Nature*, 453(7196), 770–774.

Wild, C. T., Marsh, O. J., & Rack, W. (2017). Viscosity and elasticity: A model intercomparison of ice-shelf bending in an Antarctic grounding zone. *Journal of Glaciology*, 63(240), 573–580. <https://doi.org/10.1017/jog.2017.15>

Appendix A

RTKLIB/PPP configuration

Settings	Elevation Mask	Earth Solid Tide Model	Filter Iteration	Modelling Method	Clock	Ionspheric correction	Tropospheric correction	σ (x)	σ (y)	σ (z)
1	7	Off	3	Forward	Broadcast	Boardcast	Saastamoinen	1.35	1.17	4.07
2	7	Off	3	Forward	Broadcast	IF	Saastamoinen	1.32	1.15	4.01
3	7	Off	3	Forward	Broadcast	IF	ZTD + Grad	1.31	1.14	3.99
4	15	Off	3	Forward	Broadcast	IF	ZTD + Grad	1.5	1.23	4.92
5	15	Solid/OTL	3	Forward	Broadcast	IF	ZTD + Grad	1.5	1.23	4.92
6	15	Solid/OTL	3	Combined	Broadcast	IF	ZTD + Grad	1.06	0.87	3.47
7	15	Solid/OTL	3	Combined	Precise	IF	ZTD + Grad	0.05	0.04	0.16
8	15	Solid/OTL	8	Combined	Precise	IF	ZTD + Grad	0.05	0.04	0.16

Table 4. Applied options for testing configuration in RTKLIB/PPP; σ are expressed in decimal degree and setting 8 is selected for processing in the present study.

Appendix B

Overview of GNSS processing results

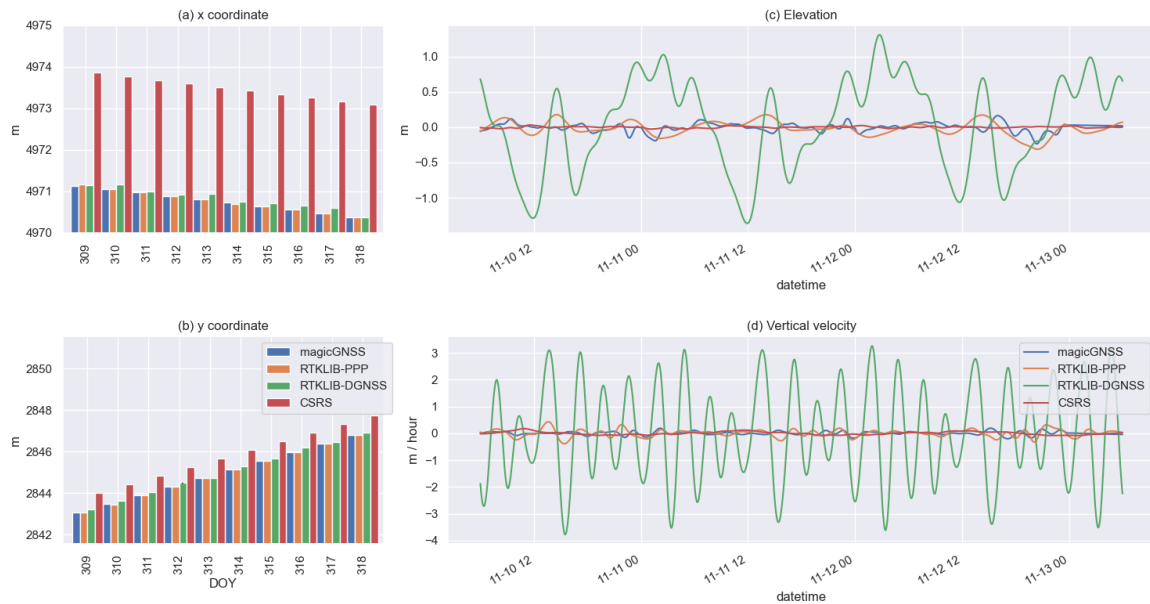


Figure 13. Positioning solutions at Blake. This figure shows positioning results using magicGNSS (blue), RTKLIB/PPP (orange), RTKLIB/DGNSS (green), and CSRS (red). (a) Daily mean x position in polar stereographic coordinates substrated from the base station; (b) Daily mean y position substrated from the base station; (c) Demeaned and detrended elevation in metres; (d) Demeaned and detrended vertical velocity in metre per hour.

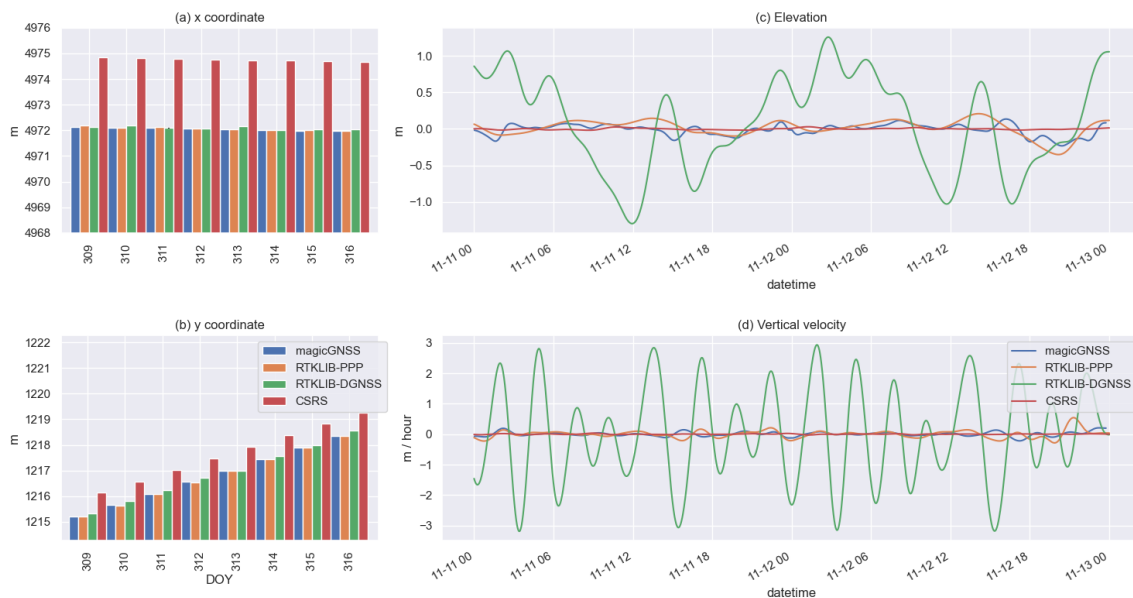


Figure 14. Positioning solutions at Hillary. This figure shows positioning results using magicGNSS (blue), RTKLIB/PPP (orange), RTKLIB/DGNSS (green), and CSRS (red). (a) Daily mean x position in polar stereographic coordinates substrated from the base station; (b) Daily mean y position substrated from the base station; (c) Demeaned and detrended elevation in metres; (d) Demeaned and detrended vertical velocity in metre per hour.

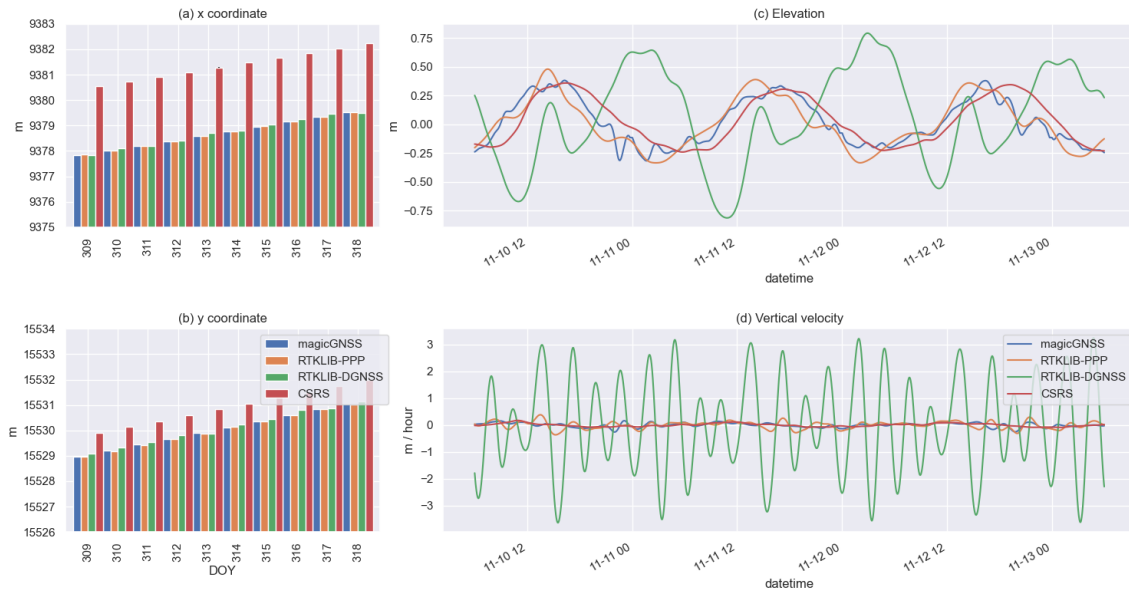


Figure 15. Positioning solutions at Shirase. This figure shows positioning results using magicGNSS (blue), RTKLIB/PPP (orange), RTKLIB/DGNSS (green), and CSRS (red). (a) Daily mean x position in polar stereographic coordinates substrated from the base station; (b) Daily mean y position substrated from the base station; (c) Demeaned and detrended elevation in metres; (d) Demeaned and detrended vertical velocity in metre per hour.



Figure 16. Positioning solutions at Tuati. This figure shows positioning results using RTKLIB/PPP (blue), RTKLIB/DGNSS (orange), and CSRS (green). (a) Daily mean x position in polar stereographic coordinates substrated from the base station; (b) Daily mean y position substrated from the base station; (c) Demeaned and detrended elevation in metres; (d) Demeaned and detrended vertical velocity in metre per hour.



Figure 17. Positioning solutions at Base. This figure shows positioning results using magicGNSS (blue), RTKLIB/PPP (orange), and CSRS (green). (a) Daily mean x position in polar stereographic coordinates substrated from the best estimates calculated using bootstrap method; (b) Daily mean y position substrated from the base station; (c) Demeaned and detrended elevation in metres; (d) Demeaned and detrended vertical velocity in metre per hour.

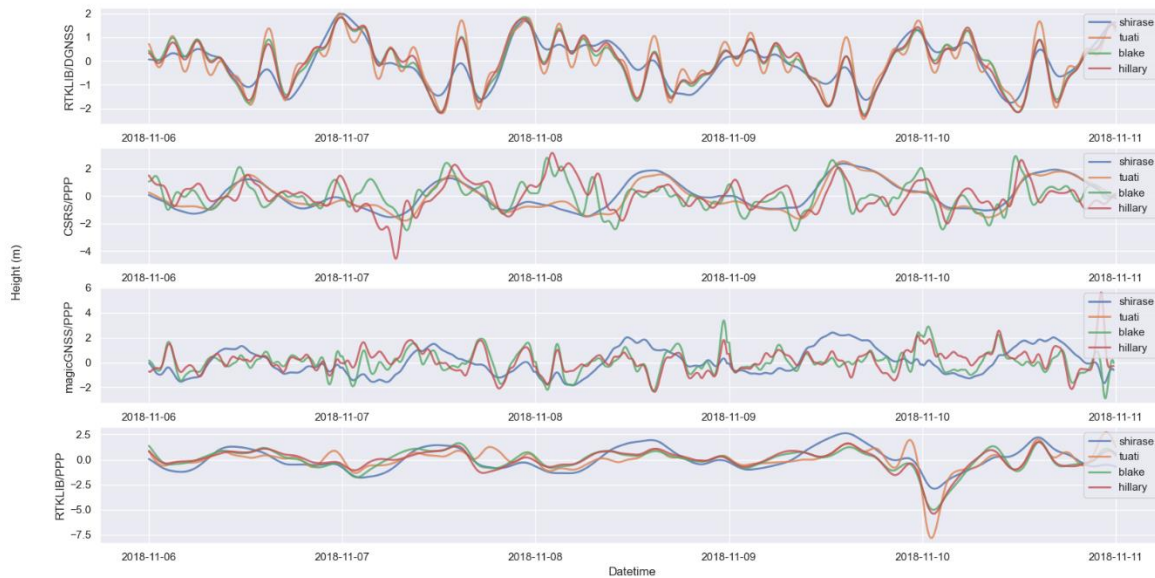


Figure 18. GNSS solutions of all stations. This figure shows positioning results of all moving stations: Shirase (blue), Tuati (orange), Blake (green) and Hillary (red), using RTKLIB/DGNSS (1st panel), CSRS/PPP (2nd panel), magicGNSS/PPP (3rd panel), and RTKLIB/PPP (4th panel).

Appendix C

Statistical information on GNSS solutions

Station	Platform/ Processing mode	x			y			z		
		μ	σ	σ^2	μ	σ	σ^2	μ	σ	σ^2
Base	CSRS/PPP	-74.371	0.009	0.000	163.308	0.008	0.000	1011.513	0.021	0.000
	RTKLIB/PPP	-74.371	0.185	0.034	163.308	0.196	0.038	1012.411	0.249	0.062
	MagicGNSS/PPP	-74.371	0.074	0.006	163.308	0.084	0.007	1011.360	0.149	0.022
Hillary	RTKLIB/DGNSS	-74.393	0.421	0.177	163.453	1.194	1.425	95.743	1.616	2.613
	CSRS/PPP	-74.393	0.062	0.004	163.453	1.029	1.058	97.275	0.028	0.001
	RTKLIB/PPP	-74.393	0.147	0.022	163.453	1.042	1.085	97.561	0.183	0.033
	MagicGNSS/PPP	-74.393	0.061	0.004	163.453	1.032	1.064	97.146	0.105	0.011
Blake	RTKLIB /DGNSS	-74.407	0.461	0.212	163.438	1.229	1.511	78.304	1.628	2.650
	CSRS/PPP	-74.407	0.221	0.049	163.438	1.074	1.153	79.750	0.021	0.000
	RTKLIB/PPP	-74.407	0.261	0.068	163.438	1.086	1.179	80.028	0.167	0.028
	MagicGNSS/PPP	-74.407	0.193	0.037	163.438	0.964	0.930	79.627	0.091	0.008
Tuati	RTKLIB /DGNSS	-74.425	0.458	0.210	163.418	1.104	1.218	62.998	1.614	2.604
	CSRS/PPP	-74.425	0.205	0.042	163.419	0.927	0.859	64.460	0.038	0.001
	RTKLIB/PPP	-74.425	0.255	0.065	163.418	0.929	0.863	64.815	0.258	0.066
	MagicGNSS/PPP	-74.425	0.334	0.112	163.418	0.603	0.364	64.761	0.581	0.337
Shirase	RTKLIB /DGNSS	-74.526	0.634	0.402	163.458	0.853	0.728	24.547	1.584	2.510
	CSRS/PPP	-74.526	0.485	0.236	163.458	0.598	0.357	26.053	0.214	0.046
	RTKLIB/PPP	-74.526	0.496	0.246	163.458	0.615	0.379	26.325	0.265	0.070
	MagicGNSS/PPP	-74.526	0.490	0.240	163.458	0.600	0.359	25.930	0.222	0.049

Table 5. Positioning statistics. This figure shows mean, standard deviation and variance of all solutions in x, y, z dimensions.

Appendix D

Results of SSA analysis

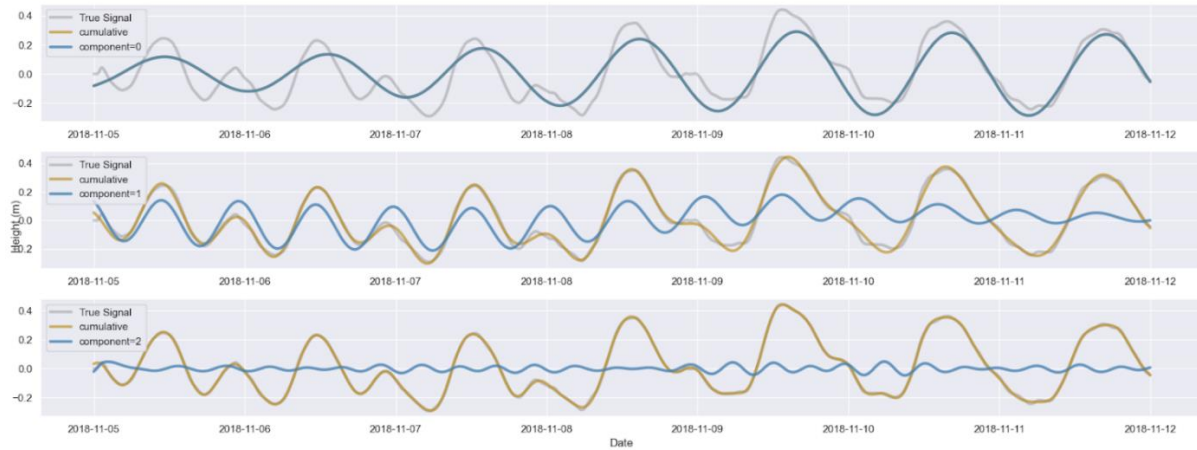


Figure 19. SSA reconstruction at Shirase. This figure shows the main three frequency components of the recorded time series using CSRS/PPP. The constituents are diurnal signals (1st panel), semi-diurnal signals (2nd panel), and residuals/ noise (3rd panel). It depicts the true signal (grey), individual component (blue) and the cumulative signal (yellow).

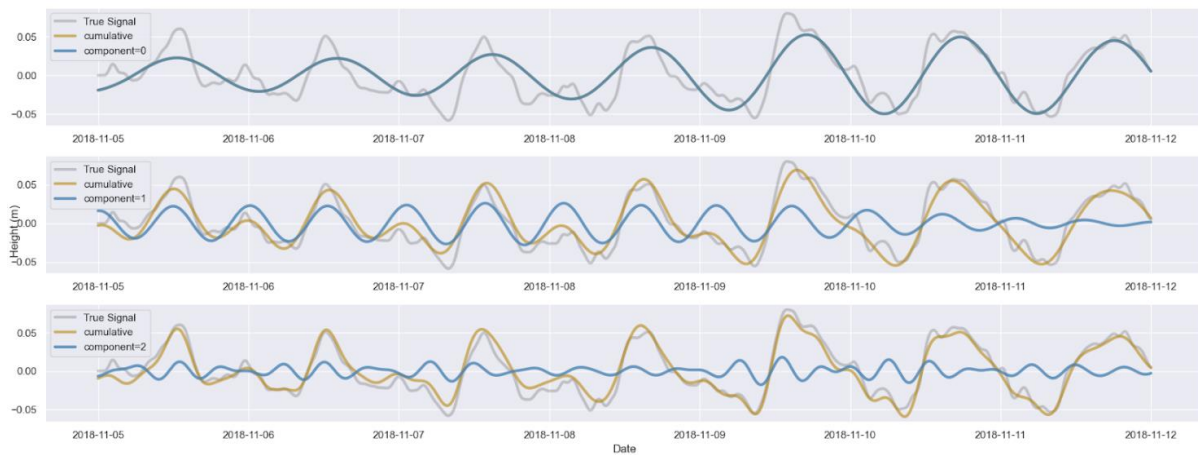


Figure 20. SSA reconstruction at Tuati. This figure shows the main three frequency components of the recorded time series using CSRS/PPP. The constituents are diurnal signals (1st panel), semi-diurnal signals (2nd panel), and residuals/ noise (3rd panel). It depicts the true signal (grey), individual component (blue) and the cumulative signal (yellow).

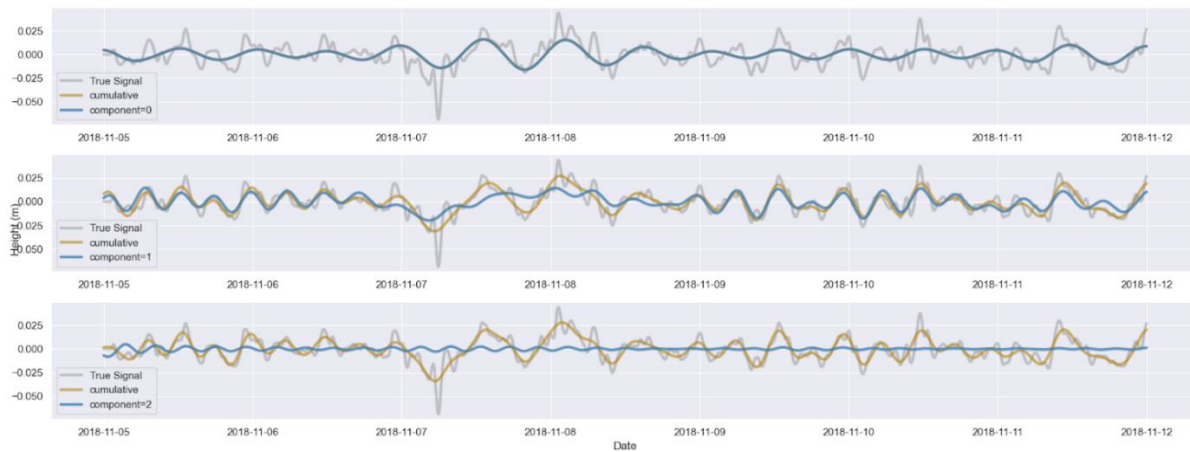


Figure 21. SSA reconstruction at Hillary. This figure shows the main three frequency components of the recorded time series using CSRS/PPP. The constituents are diurnal signals (1st panel), semi-diurnal signals (2nd panel), and residuals/ noise (3rd panel). It depicts the true signal (grey), individual component (blue) and the cumulative signal (yellow).

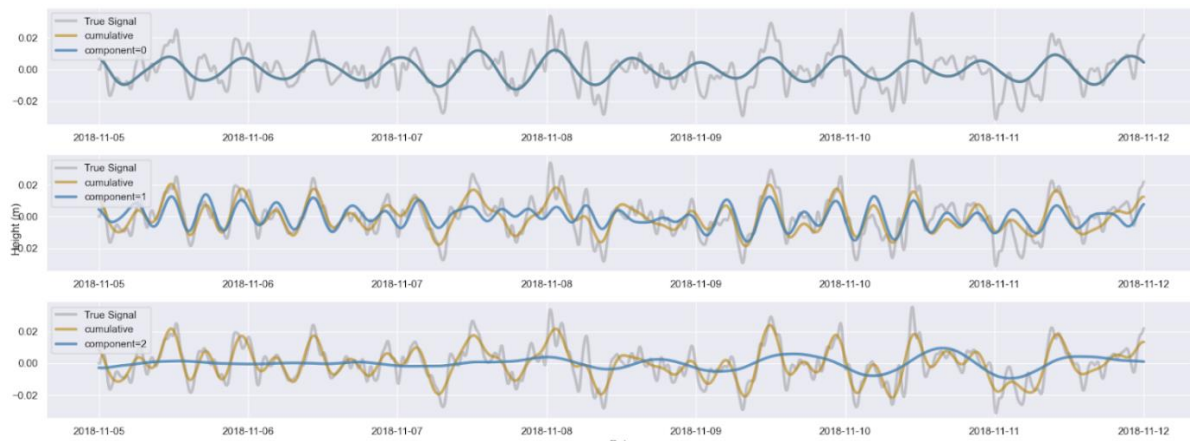


Figure 22. SSA reconstruction at Blake. This figure shows the main three frequency components of the recorded time series using CSRS/PPP. The constituents are diurnal signals (1st panel), semi-diurnal signals (2nd panel), and residuals/ noise (3rd panel). It depicts the true signal (grey), individual component (blue) and the cumulative signal (yellow).